

Excerpts from 2002 Ph.D.  
Dissertation of Dr. Justin Kasper  
MIT

## Chapter 2

# Bi-Maxwellian Analysis of Wind/SWE Ion Spectra

**ABSTRACT:** *A description of the Faraday Cup ion instruments on the Wind spacecraft. Extension of existing analysis techniques to measure the bi-Maxwellian nature of ion species. Evaluation of the analysis, comparison with other methods, instruments, and spacecraft. A brief survey of the typical properties of solar wind protons.*

### 2.1 Introduction

This chapter presents my analysis of data taken by the Faraday Cup (FC) instruments which make up the ion portion of the Solar Wind Experiment (SWE) on the Wind spacecraft [Ogilvie et al., 1995]. The data produced as a result of this analysis are the basis for the research detailed in subsequent chapters of this thesis.

The goal of SWE/FC is to characterize the bulk properties of the major ions in the solar wind, namely  $^1\text{H}$  and  $^4\text{He}$ , but also  $^3\text{He}$  in the rare situations in which it is seen. The Faraday Cups probe the three-dimensional distribution of proton and alpha particles in velocity space  $f_p(\vec{v})$  and  $f_\alpha(\vec{v})$  through measurements of the reduced distribution function (1.65). Most scientific investigations do not require this detailed information about the ion properties. As shown in Section 1.2.6 and Section 1.2.7, to first order we can describe the solar wind in as a fluid, with temperature  $T$ , velocity  $\vec{U}$ , and density  $n$  as a function of location and time. In theory calculating these contracted properties of the distribution function follows the integrals listed in Section 1.2.6. In practice the features of the instrument must be taken into account in order to produce accurate values of these “key parameters”. In this chapter the proton spectra are analyzed both through a detailed comparison of observations and a model response function, which will be referred to as the *non-linear* analysis method, and through a simplified moment routine, the *moment* analysis procedure, based on the derivations in Section 1.2.6.

The primary data products which the Wind/SWE Faraday Cups produce are the velocity, thermal speed, and density of the protons, along with the relative abundance ratio of alpha particles to the protons. John Steinberg, currently at the Los Alamos

National Laboratory, supervised the original key parameter analysis which produced the proton velocity  $\vec{V}_p$ , thermal speed  $w_p$  and density  $n_p$ , and started the analysis of helium [Steinberg et al., 1996]. The full alpha particle analysis was done by Matthias Aellig, producing the alpha velocity,  $\vec{V}_\alpha$ , thermal speed,  $w_\alpha$ , and number density  $n_\alpha$  [Aellig et al., 2001b]. I have extended our ability to characterize the ion spectra by deriving an analytical expression for the response of a Faraday Cup to the convected, field-aligned, bi-Maxwellian velocity distribution function described in Section 1.2.5. Instead of the single thermal speed  $w_p$  the parallel ( $w_{\parallel p}$ ) and perpendicular ( $w_{\perp p}$ ) thermal speeds are measured. This chapter describes this analysis of the Wind Faraday Cup proton spectra. In addition to the new response function I have introduced a new method for determining the effective collecting area of the instrument, carried out the first detailed analysis of the accuracy with which the Faraday Cup can quantify the solar wind ions, and compared the results of the non-linear and moment analysis techniques.

There are several reasons why we would like to measure anisotropies in the plasma species seen by the WIND Faraday Cup:

- Based upon the  $\chi^2$  merit function defined and discussed in Section 2.4.2, the bi-Maxwellian velocity distribution function is a more accurate description of ion species seen in the solar wind than a single isotropic Maxwellian VDF. From the simple point of view of conducting the best analysis of existing data as possible we should make the extension to a two-temperature model.
- Plasma micro-instabilities should place limits on the maximum temperature anisotropies allowed in the solar wind. Knowledge of these instabilities is of interest to the general plasma community.
- The existence of anisotropies in the ion distributions may significantly alter the results of certain analysis methods, for example in the study of collisionless magnetohydrodynamic shocks.
- Recent results with data from the SOHO spacecraft [Antonucci et al., 2000; Cranmer, 1999] suggest that extreme ion anisotropies exist in the solar corona. Anisotropies observed in the solar wind may contain information about this process and are therefore useful in the study of the corona and origin of the solar wind.

Section 2.2 describes how the Faraday Cup works and then details the derivations of FC response functions for a given velocity distribution function. The non-linear analysis algorithm is outlined in Section 2.3. In Section 2.4 the uncertainties in each of the derived parameters are explored.

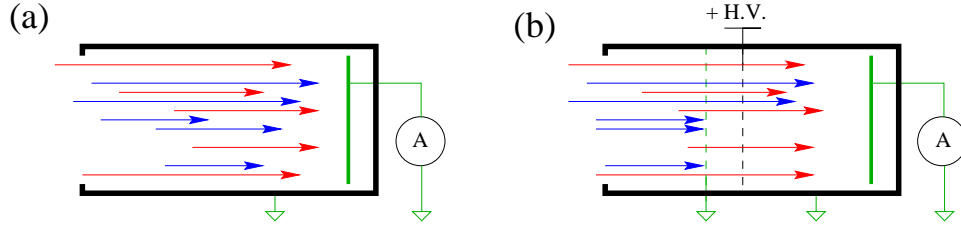


Figure 2-1: A simple cartoon showing how a Faraday Cup measures charged particle fluxes. In (a) particles of various energies (energy  $\propto$  length of arrow) and different charges (red, blue) are allowed to flow through an opening into a grounded metal container. An insulated metal plate at the back of the cup collects the particles and the total current is measured as these particles flow through the wire (green) to ground. In (b) two metal grids have been inserted into the cup. The outer grid is grounded and a voltage is applied to the inner grid to repel particles of the desired charge.

## 2.2 Faraday Cup Measurements of Ion Distribution Functions

The operating principles of a Faraday Cup are straightforward. In fact the FC is one of the few instruments for which analytic expressions may be derived for the response to a given ion distribution. Access to an analytic expression is a tremendous advantage because it allows us to compare a model distribution function with the observations and to vary the parameters of that model to produce the best agreement with the observations. As a byproduct of that analysis, we also get estimates of the uncertainty in each parameter. One of the themes of this thesis is that these uncertainties may be propagated through to any derived quantity we wish to explore, which then allows us to express a rigorous value for the statistical significance of any result.

The operational design of a Faraday Cup is outlined in Section 2.2.1, followed in Section 2.2.2 by a description of a single ion spectrum measured by the two Faraday Cup (FC) instruments on Wind. In Section 2.2.3 the response of a FC to an isotropic Maxwellian distribution function is derived. In Section 2.2.4 that response is extended to a bi-Maxwellian VDF. As a second method for analyzing FC ion spectra the moment analysis procedure is described in Section 2.2.6, and an algorithm for determining temperature anisotropies with moments is detailed in Section 2.2.7. A new method for calculating the correct effective collecting area of the FC due to the transparency of the grids is presented in Section 2.2.5.

### 2.2.1 Operational Design of the Wind/SWE Faraday Cups

The basic principle of operation of a Faraday Cup ion instrument is to measure the current produced by the flux of particles which pass through the instrument and impact one or more electrically insulated collector plates. This process is indi-

cated schematically in Figure 2-1. In the left image particles of positive and negative charges,  $q_+$ ,  $q_-$  (red and blue arrows) and varying speeds  $v_{\parallel}$  parallel to the instrument symmetry axis (proportional to the lengths of the arrows) pass through an entrance with area  $A$  and impinge upon a collector plate which is insulated from the instrument. Excess charge does not build up on the collector because it is grounded through the green wire. As current flows through the wire it is measured by an ammeter. But what is the relationship between the measured current and the VDF? If the VDF of the particles are uniform across the entrance and their average speeds and densities are  $U_{\parallel+}$ ,  $U_{\parallel-}$  and  $\rho_{\parallel+}$ ,  $\rho_{\parallel-}$ , then the measured current is,

$$I_{\text{meas}} = q_+ \rho_+ U_{\parallel+} + q_- \rho_- U_{\parallel-}. \quad (2.1)$$

The problem with this configuration is that the properties of the positive and negative particles are intertwined. Indeed, if they had the same average speeds and the plasma were neutral overall then no current would be measured. An improvement to the design is shown in the second image of Figure 2-1, in which two wire grids have been inserted within the instrument, between the entrance and the collector plate. The outer grid is grounded and a positive high voltage  $V_{\text{H.V.}}$  is applied to the inner grid relative to the instrument. This has the effect of shielding the collector plate from positively charged particles with insufficient energy to penetrate the region between the grids. A particle of mass  $m$  and charge  $q$  is reflected unless

$$\frac{\frac{1}{2} m v_{\parallel}^2}{q} \geq V_{\text{H.V.}}, \quad (2.2)$$

which now allows the FC to probe the distribution of particles  $f(v_{\parallel})$  as a function of their speed normal to the grids by varying  $V_{\text{H.V.}}$  and recording  $I_{\text{meas}}$ . There are still several aspects which need improvement. For example, photoelectrons produced by ultraviolet rays from the sun illuminating the collector plates or secondary electrons produced when a particle strikes the collector surface and subsequently escape could generate additional currents which may overwhelm the real signal. Additionally in this example the VDF of the particles which have sufficient energy to pass the high voltage grid has been altered. Still, this does illuminate the basic operating principles of a Faraday Cup. Since (2.2) does not involve the phase space density's dependence upon speeds  $\vec{v}_{\perp}$  perpendicular to the cup axis, the FC measures a quantity related to the reduced distribution function (1.65), as described in Section 1.2.6. The three-dimensional characteristics of the VDF are then resolved by placing the instrument on a rotating spacecraft. The first observations of ion fluxes in space were performed using such a Faraday Cup, with a large, fixed negative voltage to prevent the entrance of electrons into the detector [Gringauz et al., 1960]. The fixed voltage design is still used today [Němeček et al., 1997; Santolík et al., 1997], mainly due to its simplicity and ability to rapidly characterize the ions through single measurements of the flux, resulting in measurements with a high cadence [Unti et al., 1973], but at the loss of resolving the VDF.

Faraday Cups have been a workhorse for space plasma measurements for the du-

ration of *in-situ* space exploration [Vasylinuas, 1971; Gloeckler, 1990]. Over the last four decades the MIT space plasma group has developed and extended the capabilities of these instruments for exploring the heliosphere [Bridge et al., 1977; Gazis et al., 1989], by reducing their mass and power requirements, [Lazarus et al., 1993], increasing their cadence [Aellig et al., 2001a], and extracting additional information from existing observations [Richardson, 1986; Kasper et al., 2001a,b].

Many improvements may be made to the basic design, and the Faraday Cups flown on the Wind spacecraft reflect this. The design characteristics of the two Faraday Cups of the Solar Wind Experiment (SWE) on the Wind satellite are shown in Figure 2-2. There are a total of nine grids in the Wind Faraday Cups, each serving a special purpose. Instead of the pair of grounded and high voltage grids in Figure 2-1, a modulator assembly contains a high voltage grid surrounded by two ground grids. As a result, any particle which manages to pass the high voltage grid is re-accelerated to its original velocity by the time it leaves the assembly, eliminating any distortion of the original VDF. A high-voltage power supply within the instrument applies a square-wave voltage waveform to the grid at the center of the modulator. The square-wave oscillates between two high voltages,  $V_1$  and  $V_2$  at 200Hz, with  $(V_2 - V_1)/V_1 \sim 10\%$ . As shown in the figure there are three categories of particles for a given set of  $(V_1, V_2)$ : those that always reach the collector plates, those that never reach the collector plates, and those particles with parallel speeds  $V_1/q \leq 1/2mv_{\parallel}^2 \leq V_2$  which only reach the collector plates 1/2 of the time and produce a current which is modulated at 200 Hz. The exact details of the conversion of this alternating current into a measurement which is sent back down to Earth are detailed elsewhere [Ogilvie et al., 1995], but the key is that only the modulated current is recorded. This eliminates the effects of photoelectrons, solar wind electrons, and any other background signals. By stepping through increasing voltages the VDF of ions may be scanned. Two outer ground grids isolate the rest of the spacecraft from electromagnetic interference generated by the oscillating electric fields, and three inner ground grids prevent the modulator from inducing stray currents on the collector plates. A final grid, the suppressor grid, is mounted right above the collector plates and is maintained at  $-100$  volts, a sufficient amount to drive any secondary electrons back into the collector plates.

Another feature of the Wind Faraday Cups is the combination of the limiting aperture located immediately underneath the modulating assembly, and the fact that the collecting surface at the back of the instrument has been divided into two equal semi-circular plates. There is a small but treatable aberration of particles as they travel through the modulator: since the electric field is perpendicular to the grids, each particle maintains its velocity component parallel to the grids. Therefore as it is slowed down and subsequently reaccelerated in the modulator it continues to travel in the plane of the collectors. The net result is a translation of the beam of particles which is a function of their energy (in an analytic treatment it ranges from the geometrical projection at high energies to exactly twice that in the case that the particles just make it through the modulator). The limiting aperture removes this problem over a large range of angles because up to approximately  $45^\circ$  the aperture is evenly illuminated. Thus a clean circular beam is projected onto the collector plates.



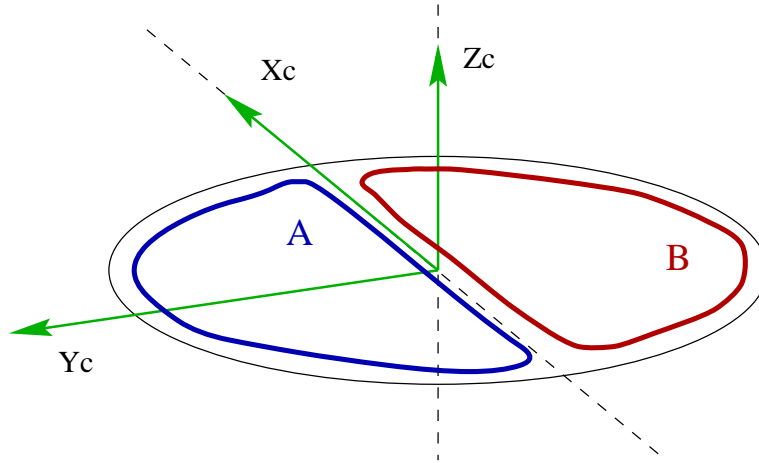


Figure 2-3: Illustration of the Faraday Cup coordinate system for the Wind instruments. The two collector plates, A and B, lie in the  $\hat{x}_c - \hat{y}_c$  plane, with  $\hat{x}_c$  directed along the split between the plates. The  $\hat{z}_c$  axis is normal to the collector plates. In subsequent discussion the “cup orientation”  $\hat{n}$  is the direction of  $\hat{z}_c$  in the GSE coordinate system.

Since the plates are split, it is then a simple matter to determine the flow angle of the incoming particles based on the relative currents seen by each plate. This allows each cup to individually determine the three dimensional properties of the solar wind ions in the event that one instrument fails. For the purposes of this thesis we will treat each FC as having a single collector plate and simply sum the two currents.

The plot in Figure 2-2 is of the effective collecting area of the instrument as a function of the angle of incidence. There are three factors which determine this. First the size of the limiting aperture, which is about 33 cm<sup>2</sup>. Second there is the transparency of the grids, which decreases very slowly from 0° to 40° but then falls off rapidly to zero. The transparency is determined by the thickness of the wires used in the grids and the average separation between wires. It can be calculated analytically and compared with observations in a calibration beam on Earth. Finally at extreme angles, greater than about 45°, the limiting aperture is no longer completely illuminated and the response becomes much more difficult to describe analytically. Numerical simulations have however yielded corrections to the effective collecting area which have been folded into the curve shown in Figure 2-2.

### 2.2.2 Description of a Single Wind/SWE Faraday Cup Spectrum

Wind rotates once every three seconds, so the following derivations of the response of a Faraday Cup to ion distributions will require transformations between the Geocentric Solar Ecliptic (GSE) coordinate system (described in Section 1.3), and the frame of the instrument. A sketch of the Faraday Cup coordinate system used in all of these



derivations is shown in Figure 2-3. A transformation matrix that converts a vector in GSE components  $\vec{V}^G$  to the frame normal to a Faraday cup on Wind,  $\vec{V}^C$ , is shown below. Call the tilt angle of each cup out of the ecliptic  $\theta$ , and the azimuthal angle in the ecliptic  $\phi$ . Define  $\phi$  as zero along  $\hat{x}_{\text{GSE}}$  and increasing towards  $\hat{y}_{\text{GSE}}$ . In component form a vector transformed into the cup frame becomes

$$\begin{aligned} V_x^C &= V_x^G \sin \phi + V_y^G \cos \phi \\ V_y^C &= V_x^G \cos \phi \sin \theta - V_y^G \sin \phi \sin \theta + V_z^G \cos \theta \\ V_z^C &= V_x^G \cos \phi \cos \theta - V_y^G \sin \phi \cos \theta - V_z^G \sin \theta \end{aligned} \quad (2.3)$$

The positions of the instruments which comprise the Solar Wind Experiment, including the two Faraday Cups, on the Wind spacecraft are shown in Figure 2-4. The spin-axis of the spacecraft, labeled “Z” in the figure, is perpendicular to the ecliptic plane of the solar system. The Faraday Cups are located  $180^\circ$  apart and look  $\pm 15^\circ$  out of the spacecraft equatorial plane, with FC1 looking slightly northward and FC2 southward. The line dividing the split collector plates also lies in the ecliptic plane, so the relative current on each plate is related to the flow angle of the solar wind out of that plane, or the “North-South” flow angle. This was done so that a single cup could extract the three dimensional solar wind parameters in the event of a failure.

Each instrument must know the azimuthal orientation of the spacecraft to a high degree of accuracy. The exact period is therefore measured on board by a sun-pulse sensor. The sensor is essentially a photodiode with a narrow field of view mounted on the side of the spacecraft, and each time that side of Wind faces the Sun it generates a pulse. A circuit tracks the average spin rate over several rotations and divides each rotation into 1000 sub-intervals. Small variations in the temperature of the spacecraft change its moment of inertia and thus alter the exact spin period.

A single ion spectrum consists of a set of measurements by the two cups of the reduced distribution function along a series of angles and over consecutive energy windows. Figure 2-5 is a diagram of the measurement sequence. A single spectrum is taken as follows: When the cups are instructed by the SWE Digital Processing Unit (DPU) to begin a spectral observation they wait until a signal is received by the Sun-sensor and then start by performing an internal calibration run for one spacecraft rotation. When the calibration is complete the high voltage power supplies on each cup are enabled and begin modulating between the first pair of voltages. Based on the timing signals from the Sun-pulse sensor the SWE DPU commands each of the two Faraday cups to perform measurements of the current at the single energy window along 20 angles. These angles may be modified through commands from the ground at any time, but they have been kept in the same location since launch: 18 angles spaced evenly at  $\sim 3.5^\circ$  intervals in  $\phi$  and two angles directed anti-Sunward, each  $35^\circ$  on either side of the  $-\hat{x}_{\text{GSE}}$  axis. Upon completion of the spin each modulator is commanded to the next higher voltage pair, and this process continues until the highest energy window is processed.

The FC high voltage power supplies produce a square-wave waveform oscillating

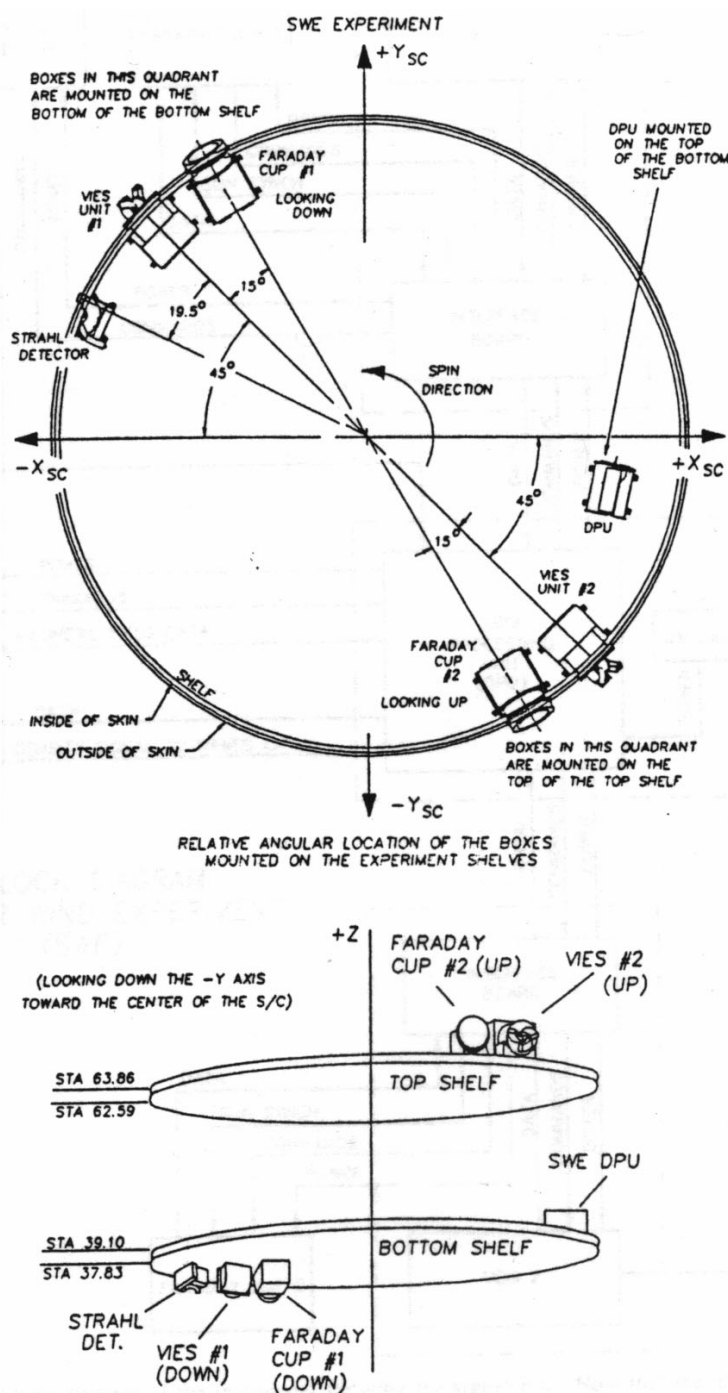


Figure 2-4: Configuration of the SWE instruments on the Wind spacecraft, adapted from [Ogilvie et al., 1995]. The two Faraday Cup ion instruments are mounted  $\pm 15^\circ$  out of the ecliptic plane, with the upper cup looking slightly northward, and the lower cup downward. Also shown are the Vector Ion-Electron Spectrometers (VEIS), the field-aligned electron Strahl detector, and the SWE DPU.

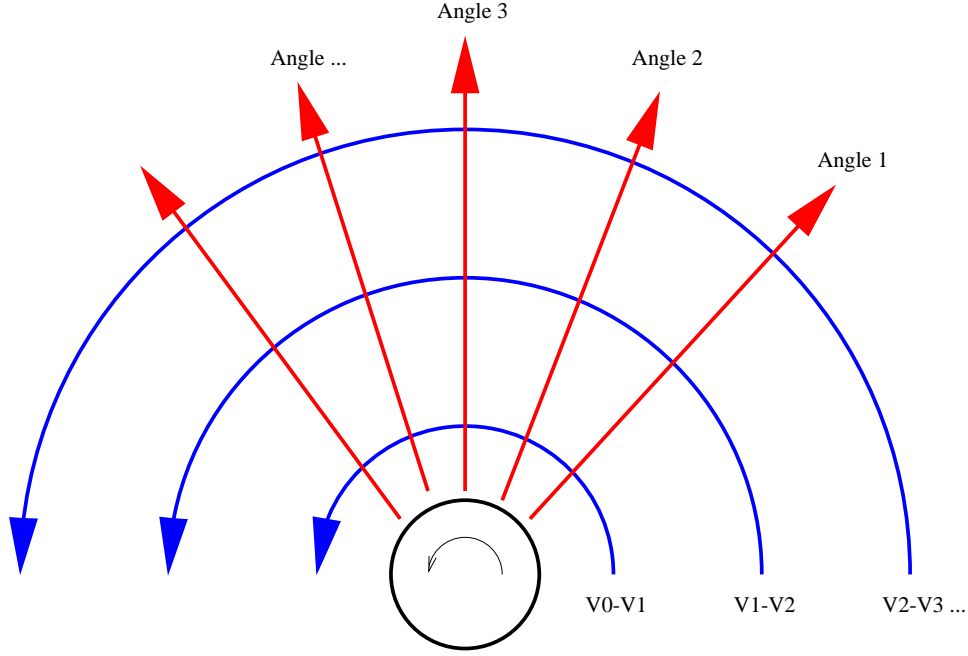


Figure 2-5: Diagram indicating the measurement of a single ion spectrum. In each single rotation the FC measures along each of the angles indicated by red arrows at a single energy window indicated by the blue arrows.

between two voltages selected from a list  $\{V_i\}$  of 64 voltages logarithmically spaced from 200 V to 8 KV, with  $\Delta V_i/V_i = (V_{i+1} - V_i)/V_i$  a constant 10%. A pair of voltages defines an energy window. There are four modes that the instruments are run in, based on the width and number of energy windows in a spectrum. Single energy windows are bounded by the voltage pair  $(V_i, V_{i+1})$ , double energy windows are twice as large, with voltages  $(V_i, V_{i+2})$ . The instrument may either conduct a full scan, stepping from the lowest to the highest energy windows, or it may “peak-track”, by only observing a subset of windows which bracket the window from the previous observation which returned the highest current. In general the Wind cups operate either in full-scan with double width energy windows or peak-track with single energy windows. The net result is that there are almost always 30 total energy windows in each spectrum.

A FC spectrum thus consists of 2400 measured currents  $I_{\text{meas}}$  as a function of the orientation of the instrument  $(\theta, \phi)$  and the location of the energy window  $(V, \Delta V)$ ,

$$2 \text{ instruments} \times 2 \text{ collectors} \times 20 \text{ angles} \times 30 \text{ windows} = 2400 \quad (2.4)$$

For this study the currents from the two collector plates in each cup are summed together, so there are 1200 measurements in a spectrum. The goal is to extract accurate and precise ion parameters from this set of currents. In the following two sections I derive the expected currents from two model ion distribution functions,

the Maxwellian and the bi-Maxwellian VDF. Once we have a relation for the model current  $I_{\text{model}}$  as a function of the model parameters and the instrument variables,

$$I_{\text{model}}[\theta, \phi, V_o, \Delta V; f_{\text{model}}(\vec{v})], \quad (2.5)$$

we can determine the parameters which produce the best fit to the observations. Section 2.2.6 describes an approximate method for extracting the same parameters for protons by calculating the moments of the observed currents.

### 2.2.3 Response to an Isotropic Maxwellian Ion Distribution

First consider the current incident on a collector plate with area  $A$  in response to an isotropic, convected Maxwellian plasma with charge  $q$ , number density  $n$ , bulk velocity  $\vec{U}$  and thermal width  $w$ . The collecting area  $A$  is a function of the size of the limiting aperture, but it additionally reflects the transparency due to the wires of the grids, so it is a function of the angle of incidence. During a single measurement, the FC high voltage modulator alternates rapidly between two voltages. These two voltages correspond to the minimum speeds,  $V_o$  and  $V_o + \Delta V_o$ , that a particle must have *normal to the grids* to pass through the modulator and impact the collector plates. The instrument returns the difference in currents observed when the grids are set to  $V_o$  and  $V_o + \Delta V$ . We can do the same by integrating over the region of velocity space which contributes to that final signal.

The differential amount of current  $dI$  produced by a small element of plasma with velocity  $\vec{v}$  in the frame of the FC (and speed  $v_z = \vec{v} \cdot \hat{z}_c$  normal to the cup) is given by

$$dI = A(\vec{v}/v)qv_z f(\vec{v})d^3\vec{v}, \quad (2.6)$$

which is a more general form of the current seen by the simple FC (2.1).

Inserting the isotropic Maxwellian distribution (1.54), the total current produced is obtained by integrating over the entire window,

$$I_{\text{iso}} = \frac{Anq}{\pi^{3/2}w^3} \iiint_{\text{window}} v_z e^{-\frac{(\vec{v}-\vec{U})^2}{w^2}} d^3\vec{v}. \quad (2.7)$$

Now we have to make two assumptions in order to get an analytical result. These are both justified because the typical ratio of the bulk speed of the ions in the frame of the Faraday Cup to the thermal width of the distribution in the solar wind is  $U/w \sim 10 - 20$ , so the ions appear from a  $2^\circ - 6^\circ$  region of the sky. The validity of this assumption is demonstrated in Figure 2-19 of Section 2.5 using the results of the analysis.

- The effective area of the instrument does not have to be folded into the integration. Instead it can be pulled out of the integral and estimated by using the angle from which the bulk of the particles contributing to the current measured in this energy window were incident. The proper subsequent calculation of the effective area is discussed in Section 2.2.5.

- When examining the current produced by a region in phase space bounded in the cup frame by  $V_z : [V_o, V_o + \Delta V_o]$ , particles in phase space with all possible velocities perpendicular to the instrument symmetry axis contribute. In reality there is a maximum possible angle of incidence into the FC, above which incoming particles are blocked. We assume here that the FC measures the current produced by an entire plane of thickness  $\Delta V_o$  in phase space.

Moving to the rest frame of the plasma by subtracting the bulk motion  $\vec{U}$  of the ions,

$$\vec{W} \equiv \vec{v} - \vec{U} \rightarrow d^3\vec{W} = d^3\vec{v}, \quad (2.8)$$

simplifying the exponential term in (2.7). With the integrals in the  $\hat{x}_c - \hat{y}_c$  frame running from  $[-\infty, \infty]$  the integral takes the form,

$$\frac{Anq}{\pi^{3/2}w^3} \int_{V_o - U_z}^{V_o + \Delta V_o - U_z} \int_{-\infty}^{\infty} \int_{-\infty}^{\infty} (W_z + U_z) e^{-(W_x^2 + W_y^2 + W_z^2)/w^2} d^3\vec{W}. \quad (2.9)$$

The exponential may be broken into three parts, and the two integrations in  $W_x$  and  $W_y$  carried out separately,

$$\frac{Anq}{\pi^{3/2}w^3} \int_{V_o - U_z}^{V_o + \Delta V_o - U_z} (W_z + U_z) e^{-(W_z^2/w^2)} dW_z \left[ \int_{-\infty}^{\infty} e^{-(W_{x,y}^2/w^2)} dW_{x,y} \right]. \quad (2.10)$$

Using the standard relation for the full integral over a Gaussian distribution,

$$\int_{-\infty}^{\infty} e^{-(x^2/\alpha^2)} dx = \alpha\sqrt{\pi}, \quad (2.11)$$

only the integration over  $W_z$  remains,

$$\frac{Anq}{\sqrt{\pi}w} \int_{V_o - U_z}^{V_o + \Delta V_o - U_z} (W_z + U_z) e^{-(W_z^2/w^2)} dW_z. \quad (2.12)$$

This can be separated into two parts by breaking up the  $V_o - U_z$  sum and writing two integrals,

$$\frac{Anq}{\sqrt{\pi}w} \left[ \int_{V_o - U_z}^{V_o + \Delta V_o - U_z} W_z e^{-(W_z^2/w^2)} dW_z + U_z \int_{V_o - U_z}^{V_o + \Delta V_o - U_z} e^{-(W_z^2/w^2)} dW_z \right]. \quad (2.13)$$

The integral on the left has an analytical solution because of the additional factor of  $W_z$  proceeding the exponential. The right integral does not, but its value may be expressed using the definition of the error function *erf*, [Abramowitz and Stegun, 1972, §6],

$$\text{erf}(x) \equiv \frac{2}{\sqrt{\pi}} \int_0^x e^{-t^2} dt = 1 - \frac{2}{\sqrt{\pi}} \int_x^{\infty} e^{-t^2} dt. \quad (2.14)$$

The solution is,

$$\frac{Anq}{\sqrt{\pi}w} \left[ -\frac{w^2}{2} e^{-w_z^2/w^2} \right]_{V_o-U_z}^{V_o+\Delta V_o-U_z} + U_z \frac{\sqrt{\pi}}{2} \text{erf} \left[ \frac{(V_o+\Delta V_o-U_z)/w}{(V_o-U_z)/w} \right]. \quad (2.15)$$

After simplification we have the model current  $I_{\text{iso}}$  a Faraday Cup would observe due to the presence of a convected, supersonic, isotropic Maxwellian particle VDF,

$$I_{\text{iso}} = \frac{ANq}{2} \left[ \frac{w}{\sqrt{\pi}} \left( e^{-(V_o-U_z)^2/w^2} - e^{-(V_o+\Delta V_o-U_z)^2/w^2} \right) + U_z \left( \text{erf} \frac{V_o + \Delta V_o - U_z}{w} - \text{erf} \frac{V_o - U_z}{w} \right) \right] \quad (2.16)$$

This formula has been used historically for fitting Faraday Cup ion spectra. The response functions derived here and in the following section are valid for any supersonic VDF ( $|\vec{U}|/w \gg 1$ ), and they are used in Chapter 4 to characterize alpha particles. The response is a function of the charge  $q$  of the species in question, and it is worth noting that an equal flux of  $^4\text{He}$  produces twice the current of protons. This response is also a function of the mass of the particles, because the relationship between the modulator voltages and the speeds corresponding to either limit of the window are functions of the charge to mass ratio of the species, as can be seen in (2.2). Thus observations of alphas and protons, which travel at approximately the same velocity in the solar wind, appear at different voltages in FC spectra (see example (b) in Figure 2-6).

## 2.2.4 Response to a Bi-Maxwellian Ion Distribution

Figure 2-6 has four examples of possible solar wind ion spectra. They are presented in the raw form in which observations by the Faraday Cups are returned to Earth: the observed current in a given energy window as a function of the energy per ion charge at which the instrument was scanning. Panel (a) is a typical spectra seen in the solar wind, with protons and alpha particles moving with approximately the same speed. The alphas appear at a higher voltage due to their larger mass per charge. The black histogram is the measured current and the blue and red curves are the model responses for protons and alphas respectively which best fit the observations.

Panel (b) of Figure 2-6 shows two measurements of the same ion distribution, but at two angles with respect to the ambient magnetic field. As we shall see this is indicative of a bi-Maxwellian distribution. This chapter details my extension of the analysis of Wind FC ion spectra by fitting the data with a model for the instrument response to convected, bi-Maxwellian velocity distribution functions (1.58) described in Section 1.2.5.

There are other departures from Maxwellian VDFs seen solar wind which will not be examined in this thesis. In Panel (c) the measured currents produced by protons are shown along two angles with respect to the magnetic field, with the black curve

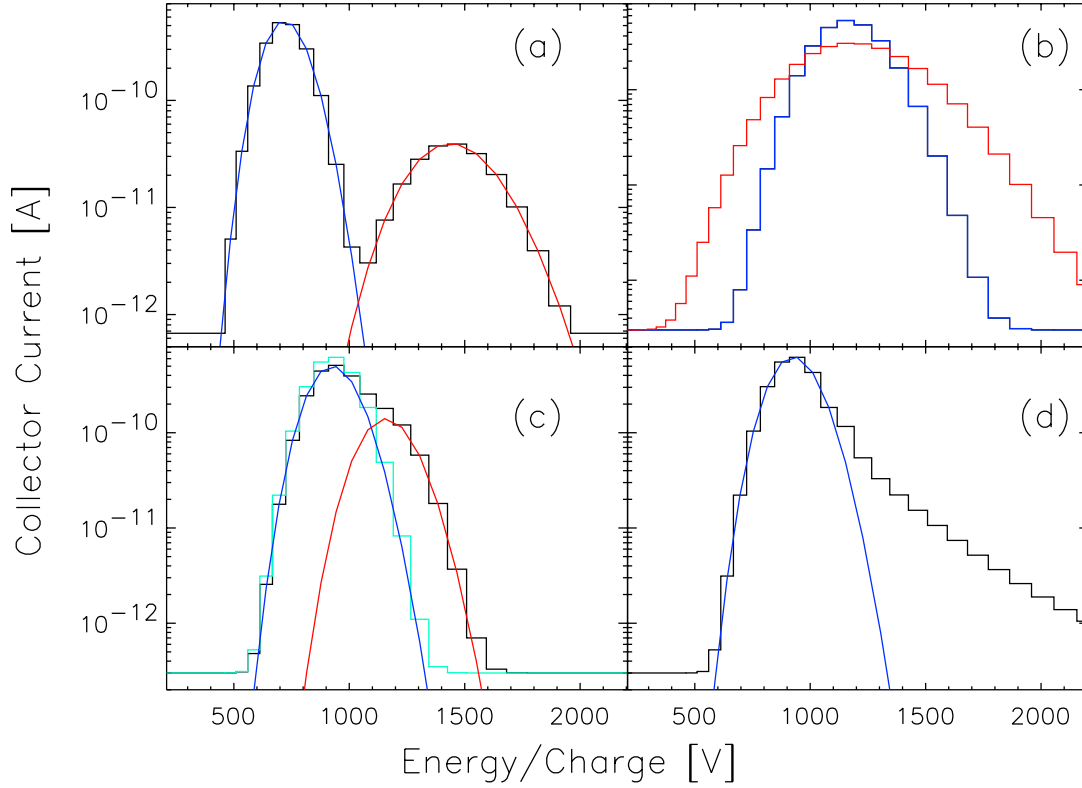


Figure 2-6: A series of examples of ion distributions as a function of energy in the solar wind. Shown are the raw currents recorded by a Faraday Cup on Wind as a function of the center voltage  $E/q$  of the window. (a) Maxwellian protons and alpha particles with approximately the same speed. The black histogram is the measured current, while the red and blue curves are the calculated currents using the derived instrument response function and the best-fit parameters; (b) A proton distribution function viewed at two angles relative to the ambient magnetic field. The red curve is from a measurement nearly along the magnetic field, while the blue curve was nearly perpendicular to the field. This demonstrates a remarkable temperature anisotropy with  $T_{\parallel p} > T_{\perp p}$ ; (c) Double double streaming: two separate, differentially streaming Maxwellian proton distributions. The red and blue curves are the predicted currents due to each of the proton distributions, and the green curve is the sum; (d) Protons with a non-Maxwellian high energy tail, which is not fit well by the model response function.

corresponding to measurements made along the field direction. It can be seen that in this case the proton distribution is actually composed of two, separate, possibly bi-Maxwellian distributions. This phenomenon is called double-streaming, and it is being investigated by Dorian Clack [Clack et al., 2001, 2002]. For example, panel (d) demonstrates the directed heat flux  $\vec{Q}$  described in Section 1.2.6.

We are now ready to derive the Faraday Cup response to a convected, field-aligned, bi-Maxwellian VDF. In addition to density and bulk velocity, there are now two thermal speeds,  $w_\perp$  and  $w_\parallel$ , perpendicular and parallel to an ambient magnetic field  $\vec{B}_0$ . The starting point is again an integration over the accessible energy window, but with a bi-Maxwellian distribution (1.58),

$$I_{\text{ani}} = \frac{Anq}{\pi^{3/2}w^3} \iiint_{\text{window}} v_z e^{-\left(\frac{v_\perp^2}{w_\perp^2} + \frac{v_\parallel^2}{w_\parallel^2}\right)} d^3\vec{v}, \quad (2.17)$$

where the collecting area has already been pulled out of the integral. In addition to the thermal speeds we must take into account the alignment of the magnetic field. The magnetic field must be transformed into the frame of the cup for each measurement through (2.3). With the unit vector  $\hat{b} = \vec{B}_0/B_0$  defining the orientation of the magnetic field seen by the cup, the integral has been simplified by the substitution

$$\vec{v}_\parallel \equiv (\vec{v} - \vec{U}) \cdot \hat{b}, \quad v_\perp \equiv (\vec{v} - \vec{U}) - [(\vec{v} - \vec{U}) \cdot \hat{b}]\hat{b} \quad (2.18)$$

The two velocities  $\vec{v}_\perp$  and  $\vec{v}_\parallel$  are the components of velocity in phase space in the rest frame of the plasma perpendicular and parallel to the magnetic field. The dependence on  $\hat{b}$  will complicate the integration, but it is still manageable. With  $\hat{b}$  in the frame of the cup we expand  $\vec{v}_\perp$  and  $\vec{v}_\parallel$ , using the same definition of  $\vec{W}$  from the previous section,

$$\begin{aligned} \vec{v}_\parallel &= W_x b_x \hat{x} + W_y b_y \hat{y} + W_z b_z \hat{z} \\ v_\parallel^2 &= W_x^2 b_x^2 + W_y^2 b_y^2 + W_z^2 b_z^2 \end{aligned} \quad (2.19)$$

and,

$$\begin{aligned} \vec{v}_\perp &= [W_x - b_x(W_x b_x + W_y b_y + W_z b_z)] \hat{x} \\ &\quad + [W_y - b_y(W_x b_x + W_y b_y + W_z b_z)] \hat{y} \\ &\quad + [W_z - b_z(W_x b_x + W_y b_y + W_z b_z)] \hat{z}. \end{aligned} \quad (2.20)$$

The magnitude of  $\vec{V}_\perp$  is

$$\begin{aligned} \vec{v}_\perp \cdot \vec{v}_\perp &= (1 - b_x^2)W_x^2 + (1 - b_y^2)W_y^2 + (1 - b_z^2)W_z^2 \\ &\quad - 2b_x b_y W_x W_y - 2b_x b_z W_x W_z - 2b_y b_z W_y W_z. \end{aligned} \quad (2.21)$$

The additional assumption of this expansion is that  $\hat{b}$ , in addition to the ion VDF, does not vary over the course of the measurement. Substituting these expressions for



$v_\perp^2$  and  $v_\parallel^2$  back into (2.17), the integral takes the slightly longer form,

$$\begin{aligned}
I = & \frac{Anq}{\pi^{3/2} w_\perp^2 w_\parallel} \int_{V_o - U_z}^{V_o + \Delta V_o - U_z} dW_z \int_{-\infty}^{\infty} dW_x \int_{-\infty}^{\infty} dW_y (W_z + U_z) \cdot \\
& \text{Exp} \left( - \left[ (1 - b_x^2) W_x^2 + (1 - b_y^2) W_y^2 + (1 - b_z^2) W_z^2 \right. \right. \\
& \quad \left. \left. - 2b_x b_y W_x W_y - 2b_x b_z W_x W_z - 2b_y b_z W_y W_z \right] / w_\perp^2 \right. \\
& \quad \left. - \left[ b_x^2 W_x^2 + b_y^2 W_y^2 + b_z^2 W_z^2 + 2b_x b_y W_x W_y + 2b_x b_z W_x W_z \right. \right. \\
& \quad \left. \left. + 2b_y b_z W_y W_z \right] / w_\parallel^2 \right). \tag{2.22}
\end{aligned}$$

While the term in the exponential has a more complex form than the isotropic Maxwellian case, the integration is still straightforward. The final result for the current  $I_{\text{ani}}$  due to a supersonic convected bi-Maxwellian VDF is,

$$\begin{aligned}
I_{\text{ani}} = & \frac{Anq}{2} \left[ \frac{\tilde{w}}{\sqrt{\pi}} \left( e^{-(V_o - U_z)^2 / \tilde{w}^2} - e^{-(V_o + \Delta V_o - U_z)^2 / \tilde{w}^2} \right) \right. \\
& \left. + U_z \left( \text{erf} \frac{V_o + \Delta V_o - U_z}{\tilde{w}} - \text{erf} \frac{V_o - U_z}{\tilde{w}} \right) \right], \tag{2.23}
\end{aligned}$$

where now there is an effective thermal speed  $\tilde{w}$  which is a function of the orientation of the magnetic field with respect to the cup,

$$\tilde{w} \equiv \sqrt{b_z^2 w_\parallel^2 + (b_x^2 + b_y^2) w_\perp^2} = \sqrt{b_z^2 w_\parallel^2 + (1 - b_z^2) w_\perp^2} \tag{2.24}$$

By virtue of the fact that the Faraday Cup measures the reduced distribution function, a bi-Maxwellian VDF looks exactly like an isotropic Maxwellian, with an effective thermal speed determined through a simple projection. Note that  $\tilde{w}$  only depends on the projection of the field parallel and perpendicular to the cup, and not on the specifics of the field orientation in the cup's  $\hat{x}_c - \hat{y}_c$  plane. This result is due to our approximation of the cup as having infinite response in velocity space perpendicular to the collector plates and because we are summing the currents measured by the individual plates in each cup.

We can make a few checks to verify that (2.23) holds under simplifying circumstances.

- **Magnetic field points straight into the Faraday cup**

In this case  $b_x$  and  $b_y$  are both zero, and the effective thermal speed reduces to  $\tilde{w} = w_\parallel$ , as expected.

- **Magnetic field is aligned parallel to the collectors**

If  $b_x^2 + b_y^2 = 1$ , then there is no  $b_z$  component and  $\tilde{w}$  reduces to  $w_\perp$ .

- **There is no anisotropy**

We have  $w_\perp = w_\parallel = w$ . Therefore

$$\tilde{w} = \sqrt{b_z^2 w^2 + (b_x^2 + b_y^2) w^2} = w \sqrt{b_x^2 + b_y^2 + b_z^2} = w \quad (2.25)$$

### 2.2.5 Choice of Effective Collecting Area for bi-Maxwellian Distribution

In the derivations of the Faraday Cup response functions to isotropic and anisotropic Maxwellian distribution functions the effective area  $A$  was pulled out of the integral over the energy window. This approximation is justified because  $A$  is a slowly varying function of the angle of incidence and because the phase space density is sharply peaked at a single point in the energy window. The VDF will indeed be peaked, both because we are dealing with Gaussian quantities and because the Mach number of the solar wind is very high.

The variation of the effective collecting area as a function of the angle of incidence has been both derived analytically and determined through numerical simulations. The two dominant effects are the varying transparency of the wires which comprise the various grids in the cup, and blocking of the limiting aperture under extreme angles of incidence. Therefore for the purposes of this section  $A(\theta)$  is taken as a given, where  $\theta$  is the angle of the incident particles relative to the cup normal. Increasingly sophisticated methods for calculating  $\theta$  are now presented, starting with the original key parameter analysis, the algorithm used for the isotropic alpha-proton analysis [Aellig et al., 2001b], and ending with a new derivation for an anisotropic VDF.

The original key parameter algorithm used a fixed value for  $A$  corresponding to its maximum value of 33.8 cm<sup>2</sup> at normal incidence ( $\theta = 0$ ). The non-linear code developed by Aellig for the isotropic analysis of the protons and alphas used the angle between the cup orientation  $\hat{n}$  and the bulk flow  $\vec{U}$  (for this section  $\vec{U}$  is in the frame of the FC),

$$\theta = \cos^{-1} \frac{U_z}{|\vec{U}|}. \quad (2.26)$$

Consider the two example proton velocity distribution functions (a) and (b) shown in Figure 2-7 in the rest frame of a Faraday Cup.  $V_\perp$  is the speed perpendicular to the cup normal, and  $V_\parallel$  is the speed along the normal axis. The shaded ellipses represent the phase space density of the protons, with the rainbow coloring indicating six thermal widths from the peak. Both VDF have the same bulk velocity  $\vec{U}$  and density  $n$ , but in (a) the distribution is isotropic with  $w = 30$  km/s, while in (b) it is anisotropic, with thermal speeds  $w_\perp = 30$  km/s and  $w_\parallel = 60$  km/s aligned with the field orientation indicated by the black arrow. The solid blue lines indicate the 45° angle of incidence to the FC at which the effective area begins to drop

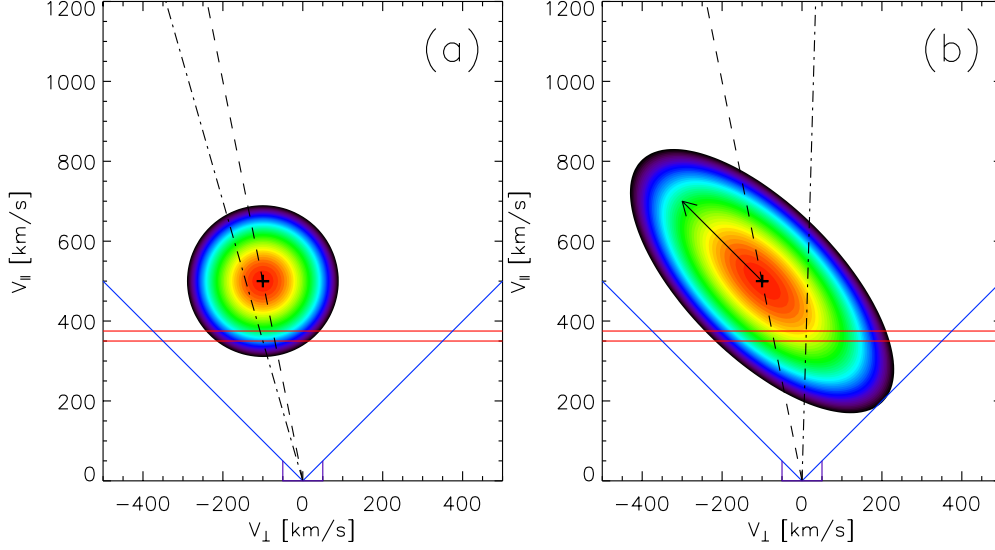


Figure 2-7: Two example distributions in velocity space. *Left:* An isotropic velocity distribution function with a single thermal speed of 30 km/s. *Right:* An anisotropic VDF with  $w_{\perp} = 30$  km/s and  $w_{\parallel} = 60$  km/s, and magnetic field orientation indicated by the black arrow. In both images the cross identifies the maximum density of the VDF, the solid red lines indicate the selected velocity window, the blue lines are the nominal field of view of the instrument, the dashed line connects the origin to the point in the VDF with maximum density, and the dotted-dashed line connects the origin to the point in the energy window with the highest density. It is clear from this example that for an anisotropic distribution we need a better way of determining the angle of incidence than the historical technique.

rapidly, and the two solid red lines mark the upper and lower boundaries of the energy window which we shall now consider. It is clear that for this example the supersonic distributions fit entirely within the region of the energy window seen by the cup. The crosses indicate the location of the bulk velocity of the plasma in each panel, and the dashed lines show the angle determined by (2.26). The dotted-dashed lines are the line from the origin to the actual location of the point in the energy window which contributes the most to the total flux in this measurement.

In the case of the isotropic VDF in Figure 2-7, the difference between the two angles is due to the fact the maximum current in the window does not necessarily come from the same angle as the bulk flow. So the first correction, which works at least for isotropic distributions, is to use the speed  $V_o$  of the window instead of the

component of the bulk speed normal to the cup,  $U_z$ ,

$$\theta = \cos^{-1} \frac{V_o}{|\vec{U}|}. \quad (2.27)$$

In the case of the anisotropic distribution in (b) however, even (2.27) produces the wrong angle. In fact, both (2.26) and (2.27) may be off by a great deal in the case of large temperature anisotropies. The solution is to derive the location of the point in phase space  $(V_x^{\max}, V_y^{\max}, V_z^{\max})$  for a bi-Maxwellian distribution function with the maximum density in a specified velocity window. Under the assumption that  $\Delta V_o/V_o \ll 1$ ,  $V_z^{\max} \simeq V_o$ , so the problem is now two-dimensional. Start with a differential form of the original anisotropic response equation (2.17),

$$\frac{dI}{d^3\vec{v}'} = \frac{ANq}{\phi^{3/2}w_{\perp}^2w_{\parallel}}(\vec{v}' \cdot \hat{n})e^{-(v_{\perp}^2/w_{\perp}^2 + v_{\parallel}^2/w_{\parallel}^2)}, \quad (2.28)$$

where through (2.18)  $v_{\perp}$  and  $v_{\parallel}$  are functions of  $\hat{b}$  and  $\vec{U}$ . Since variations normal to the cup are being neglected,  $\vec{v}' \cdot \hat{n}$  is a constant. The collecting area  $A$  varies slowly over the range in angles we are considering (in the analysis of a single ion spectrum we will discard point at large angles of incidence). So defining  $R$  as the natural logarithm of (2.28) and discarding the area term and any constants,

$$R \equiv -\ln \frac{dI}{d^3\vec{v}'} \propto \frac{v_{\perp}^2}{w_{\perp}^2} + \frac{v_{\parallel}^2}{w_{\parallel}^2}. \quad (2.29)$$

Now it is just a matter of finding the  $(V_x^{\max}, V_y^{\max})$  which maximizes  $R$  for a given  $\vec{U}$ ,  $\hat{b}$ ,  $w_{\perp}$ , and  $w_{\parallel}$ . This is done by differentiating  $R$  with respect to  $V_x$  and  $V_y$  and identifying the point  $(V_x^{\max}, V_y^{\max})$  where it vanishes. After some algebra,

$$\begin{aligned} v_x^{\max} &= U_x - \frac{b_x b_z (v_z - U_z)(w_{\perp} - w_{\parallel})(w_{\perp} + w_{\parallel})}{b_z^2 w_{\parallel}^2 + (1 - b_z^2)w_{\perp}^2} \\ v_y^{\max} &= U_y - \frac{b_y b_z (v_z - U_z)(w_{\perp} - w_{\parallel})(w_{\perp} + w_{\parallel})}{b_z^2 w_{\parallel}^2 + (1 - b_z^2)w_{\perp}^2}, \end{aligned} \quad (2.30)$$

and the angle of incidence used for the analysis of anisotropic distributions is

$$\theta = \cos^{-1} \frac{V_o}{\sqrt{(V_x^{\max})^2 + (V_y^{\max})^2}}. \quad (2.31)$$

## 2.2.6 Moments of Faraday Cup Spectra

In Section 2.2.3 and Section 2.2.4 we explicitly derived the response of a FC instrument to convected supersonic Maxwellian and bi-Maxwellian ion velocity distributions. Section 2.3 discusses the *non-linear* analysis technique, in which these models are compared with observations to produce a set of ion parameters which give the

best fit to the data. The current section presents a routine for estimating the bulk properties in the solar wind by following the methods described in Section 1.2.6 for collapsing the details of the VDF. This is called the *moment* analysis technique. There are several good reasons to pursue the moment analysis as well as the non-linear method: It is a good consistency check on both methods, and the moments provide an easy visualization of the FC observations of the anisotropies. Additionally, moments are a common method used by investigators to characterize the properties of ions and electrons in the solar wind. As will be seen, the non-linear technique is far more robust and provides much more information about the VDF. Generally the moments are used because of their simplicity, but also because it is not possible in general to produce the same analytic expressions developed in the previous sections for all instrument types. Since there has been a great deal of discussion of differences in solar wind parameters reported by different investigations, which generally involve non-linear analysis of Faraday Cup data and moment analysis of another class of ion instruments, electrostatic analyzers, it is important to apply both methods to the same dataset. In Section 2.4.4 the two techniques are compared and the sources of discrepancies are identified.

The current seen by a FC oriented in the direction  $\hat{n}(\theta, \phi)$  and scanning in the window  $(V_o, V_o + \Delta V)$  is the integration over (2.6),

$$dI = A(\vec{v}/v)q v_z f(\vec{v}) d^3\vec{v}. \quad (2.32)$$

The FC measures the reduced distribution function (1.65), so with  $\bar{A}$  representing the appropriate value for  $A(\vec{v}/v)$ , which will be determined once we know the bulk velocity of the protons, we write the differential current

$$dI = \bar{A} q v_z f(v_z) dv_z \quad (2.33)$$

as a one-dimensional problem. The most significant approximation of the moment analysis technique is that  $f(v_z)$  does not vary much over the width of the speed window  $\Delta V$ , so we may approximately write the total current  $\Delta I$  as

$$\Delta I \simeq \bar{A} q v_z f(v_z) \Delta V. \quad (2.34)$$

The phase space density  $f_i$  of the reduced distribution function along  $\hat{n}$  for the  $i^{\text{th}}$  window at  $(V_i, \Delta V_i)$  is then approximately

$$f_i = \frac{\Delta I_i}{\bar{A} q V_i \Delta V_i}. \quad (2.35)$$

There are several problems with this treatment. First,  $f(v_z)$  is a rapidly varying function of  $v_z$ , so the approximate integral will be in error. By simply normalizing the current by  $\Delta V_i$  we have not weighted each part of the energy window correctly. Additionally, we have assumed that all particles move with speed  $V_i$  in determining  $f_i$  and we know that  $\Delta V_i/V_i \simeq 10\%$ . Expecting errors on the order of several percent, we can still proceed to calculate proton parameters. Assuming that the entire VDF

is in the energy range swept out by the FC in this spectrum, the apparent proton number density along this angle  $n(\hat{n})$  is just the sum of  $f_i$  over all measurements in this direction,

$$n(\hat{n}) = \sum_i \frac{\Delta I_i}{\bar{A} q V_i \Delta V_i}. \quad (2.36)$$

In a similar manner to (1.62), the average speed of the distribution viewed in this direction,  $U(\hat{n})$ , is

$$U(\hat{n}) = \frac{1}{n(\hat{n})} \sum_i f_i V_i. \quad (2.37)$$

Following (1.63) and the fact that in the previous section it was shown that even the bi-Maxwellian distribution will appear isotropic when viewed in a single arbitrary direction, we write the effective thermal speed  $w(\hat{n})$ ,

$$w(\hat{n}) = \sqrt{2} \left( \frac{\sum_i f_i (V_i - U(\hat{n}))^2}{n(\hat{n})} \right)^{1/2}. \quad (2.38)$$

Typically the moments may be calculated along 20 to 30 of the angles in a spectrum, so there are many measurements of the projection  $U(\hat{n}) = \vec{U} \cdot \hat{n}$  of the bulk velocity vector  $\vec{U}$  into the cup frame. The projection effect is linear, so we have an over-determined set of equations which can be inverted to determine the bulk velocity. The Singular Value Decomposition (SVD) method is used to determine  $\vec{U}$  [Press et al., 1999, §2.6].

Finally, the value of  $\vec{U}$  is used to renormalize the apparent density  $n(\hat{n})$  by taking into account the change of the effective area with angle of incidence,  $\theta = \cos^{-1} \vec{U} \cdot \hat{n} / U$ , and produce a corrected proton number density,  $n_c$ ,

$$n_c(\hat{n}) = \frac{A(\theta)}{\bar{A}} n(\hat{n}). \quad (2.39)$$

It is worth mentioning that the moment determinations were not dependent on the actual number density along a given angle as long as  $A$  is not a noticeable function of the speed of the energy window.

In the standard moment analysis the proton density and thermal speeds are given by the average values of  $n_c(\hat{n})$  and  $w(\hat{n})$  over all angles, and the deviation of these quantities is an estimate of their uncertainty. The following section outlines the method for determining the temperature anisotropy from  $w(\hat{n})$ .

### 2.2.7 Temperature Anisotropy with Moments

It was shown that observations of a bi-Maxwellian VDF by a Faraday Cup appear isotropic along a given angle (2.23). The simple form of the projected effective thermal speed  $\tilde{w}$  in (2.24) suggests that the thermal speeds  $w(\hat{n})$  calculated by the moment

analysis may be used to determine the parallel and perpendicular thermal speeds.

The Sunward-facing component of a spectrum contains scans through the proton VDF at 36 ( $2 \text{ cups} \times 18 \text{ angles}$ ) angles relative to the magnetic field. Starting with  $w(\hat{n})$  and the average background magnetic field  $\vec{B}_o$ , we fit

$$\tilde{w}(\hat{n}) = \sqrt{(\hat{b} \cdot \hat{n})^2 w_{\parallel}^2 + (1 - (\hat{b} \cdot \hat{n})^2) w_{\perp}^2} \quad (2.40)$$

to the observations with  $w_{\perp}$  and  $w_{\parallel}$  as free parameters.

If the moment and non-linear results agree this will be a good demonstration of the robustness of the ability of a FC to measure anisotropies. There are two cases that could create a disagreement between the results, but this difference could be useful in highlighting intervals in the solar wind which merit further study. In certain cases, especially in the high speed coronal solar wind, the proton VDF generally takes the form of two separate bi-Maxwellian distributions, with a differential flow speed aligned with the magnetic field. Sometimes the solar wind ions possess an appreciable heat flux, which is also directed along the magnetic field. In both of these cases one would expect the moment parallel thermal speed,  $w_{\parallel \text{mom}}$  to be greater than the non-linear parallel thermal speed,  $w_{\parallel \text{nl}}$ .

## 2.3 Outline of Analysis Procedure

This section is an outline of how the methods developed in Section 2.2 are applied to the ion spectra. In Chapter 4 this routine is extended to include the analysis of alpha particles. The procedure has also been modified to characterize the nature of double streaming protons in the solar wind [Clack et al., 2002].

### 2.3.1 Preparation of a Single Ion Spectrum

The spacecraft spin rate and the number of energy windows in the spectrum are used to calculate the duration of the observation, which on average is 92 seconds. The set of three-second vector magnetic field measurements provided by the MFI investigation which were made during this observation period are collected and the average ambient magnetic field  $\vec{B}_o$  is calculated,

$$\vec{B}_o \equiv \frac{\sum_i^N \vec{B}_i}{N}, \quad (2.41)$$

along with the deviation of the magnitude of the three-second field measurements,  $\Delta B$ , and the angular fluctuation of the direction of the field,  $\Delta\theta_B$  over the course of the ion spectrum,

$$\Delta\theta_B \equiv \text{Std. Dev} \left( \cos^{-1} \frac{\vec{B}_i \cdot \hat{b}}{|\vec{B}_i|} \right). \quad (2.42)$$

The direction of the field normal,  $\hat{b}$ , is then calculated in the frame of each of the  $\sim 1200$  individual measurements in the spectrum through the transformation matrix (2.3), under the assumption that the direction does not change much over the duration of the observation. The validity of this assumption is assessed in Section 2.4.4.

### 2.3.2 Moment Analysis of the Proton Distribution

The moments described in Section 2.2.6 are calculated using data selected from each angle in the spectrum. The data selection proceeds as follows independently for each angle. The speed window  $V$  with the largest current  $I_{\max}$  (and corresponding flux  $f_{\max}$ ) is identified. All measurements with speeds within  $V/2$  of  $V$ , fluxes greater than 1% of  $f_{\max}$ , and currents greater than  $1 \cdot 10^{-12}$  A (compare to the instrumental background current  $\sim 2 \cdot 10^{-13}$  A) are selected. The moments are then calculated along every angle that has at least three selected measurements, yielding  $w(\hat{n})$ ,  $n(\hat{n})$ , and  $U(\hat{n})$ . Application of the SVD algorithm to the  $U(\hat{n})$  produces the bulk velocity  $\vec{U}$ , which is then used to correct the number densities with a better estimate of the effective area. Since the anisotropy of the protons is not known we cannot use (2.31). The moments are calculated over the entire distribution function, so (2.27) is also not well defined. The best that can be done is to use the bulk velocity and (2.26).

Figure 2-8 is a plot of  $n(\hat{n})$  as a function of the angle between  $\hat{n}$  and the bulk velocity  $\vec{U}$  using the moments of a spectrum observed by Wind in the solar wind at 2032 UT on November 3, 1998. The number densities determined by each cup are shown, after the correction to the effective area to reflect the flow angle relative to the cup, with diamonds for FC1 and crosses for FC2. Note the large drop in the calculated number density for angles greater than about  $35^\circ$ . The drop is due to several effects including the rapid change in the effective area which begins near this angle of incidence and the possibility that a portion of the proton VDF is no longer in the field of view of the FC. The median value of the 20 largest densities is calculated, and all measurements of  $n(\hat{n})$  within 5% of that value measured at angles less than  $40^\circ$  from the bulk flow of the plasma are selected for subsequent analysis. The selected points in the spectrum displayed in the figure are shown with solid symbols, while the grey symbols indicate density measurements discarded as suspicious. The moment number density is the average of the selected values.

The top panel of Figure 2-9 shows the moment determination of the proton thermal speed  $w(\hat{n})$  as a function of the angle between the cup orientation  $\hat{n}$  and the average direction of the magnetic field  $\hat{b}$  for the same spectrum. The points which are shown as grey symbols correspond to the same points from the previous figure which were discarded as having suspicious number densities. Note the remarkably linear dependence of  $w(\hat{n})^2$  on  $\hat{b} \cdot \hat{b}$ , in agreement with the prediction of (2.24). The over-plotted line is the result of a robust straight-line fit [Press et al., 1999, §15.7] of (2.24) to the observations. The values of  $w_\perp$  and  $w_\parallel$  which produced the best fit to the observations are listed in the plot, along with the percent error of the fit (The percent error is the best estimate of the quality of the fit possible because we do not know the uncertainties of each moment determination of the thermal speed). For this spectrum  $w_\parallel > w_\perp$ . The bottom panel of Figure 2-9 is an example of a proton



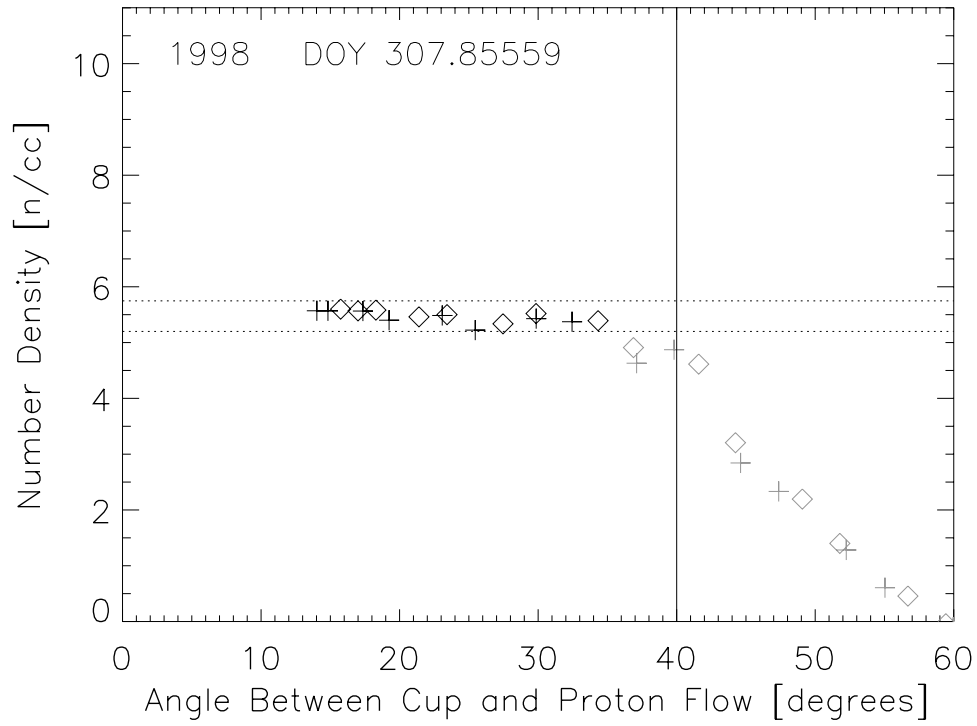


Figure 2-8: An example of the selection of FC angles  $\hat{n}$  for a single spectrum to be used for moment determination of density and thermal anisotropy. The number densities determined by each cup are shown, with diamonds for FC1 and crosses for FC2. All points indicated by grayed symbols are discarded from the subsequent analysis because they have a flow angle of greater than  $40^\circ$  from the cup normal or erroneous densities.

spectrum with  $w_{\parallel} > w_{\perp}$ .

The optimum limits for data selection and the fitting routine for the anisotropy analysis of the moment data were developed by an undergraduate in the group, James Tanabe [Tanabe et al., 2001], in parallel with my development of the non-linear analysis. Once we had generated plots of  $w(\hat{n})^2$  vs  $\hat{b} \cdot \hat{b}$  it was clear that the Faraday Cup can indeed make robust measurements of the proton temperature anisotropy.

### 2.3.3 Initial Guess

An initial guess for the parameters of the proton distribution is needed for the selection of data and as input to the fitting routine. The free parameters are  $U_x, U_y, U_z, w_{\perp}, w_{\parallel}$ , and  $n_p$ . If the moment analysis succeeded and produced “reasonable” proton parameters then it is used as the initial guess. A reasonable set of parameters is defined as being supersonic ( $U/w_{\perp} > 1, U/w_{\parallel} > 1$ ), with realistic velocity  $U_x < 0, 200 \leq U \leq 1200$ , and density  $0.01 \leq n_p \leq 300$ .

If the moment analysis was not successful, or the moment parameters are judged to be questionable, then the initial guess is formed directly from the raw currents. It is assumed that the flow is radial, so  $U_y$  and  $U_z$  are both zero. The bulk speed  $U$  is estimated as the speed of the window with the highest current, and  $U_x = -U$ . A mach number of 10 is assumed, so both  $w_{\perp}$  and  $w_{\parallel}$  are set to  $U/10$ . A fixed number density of 10 protons  $\text{cm}^{-3}$  is used because the fitting procedure is the least sensitive to the initial guess of the density.

### 2.3.4 Selection of Proton Data

Individual measurements from the two cups are selected for comparison with the bi-Maxwellian model based upon the initial guess proton parameters. It is important that only currents due to the protons are included in this set, as the inclusion of currents due to effects not accounted for in the model will contaminate the results of the fit. From experience, contamination will effect the bulk velocities least, followed by the number density. The thermal widths are the most sensitive to the inclusion of observations which are inconsistent with the model. Measurement selection is dictated by the four parameters **ANGLEMAX**, **THERMALMAX**, **CURRMIN**, and **PEAKFRAC**, which are now described and justified. The final values of the parameters were determined in a procedure described in Section 2.4.1 and their values are listed in Table 2.1

There are two contamination sources, physical and model/instrumental. Physical factors include the presence of alpha particles, a second proton distribution, or a non-negligible proton heat flux. To avoid substantial contamination from alpha particles the parameter **THERMALMAX** is the maximum number of thermal widths above and below the projected proton speed along each angle in which the selected data must fall. The effective thermal speed is calculated along each angle based on the magnetic field orientation and the current values of the parallel and perpendicular thermal speeds. The effect of non-Maxwellian characteristics like heat flux are limited in part by only taking measurements with currents greater than **PEAKFRAC** times the maximum current in the spectrum.

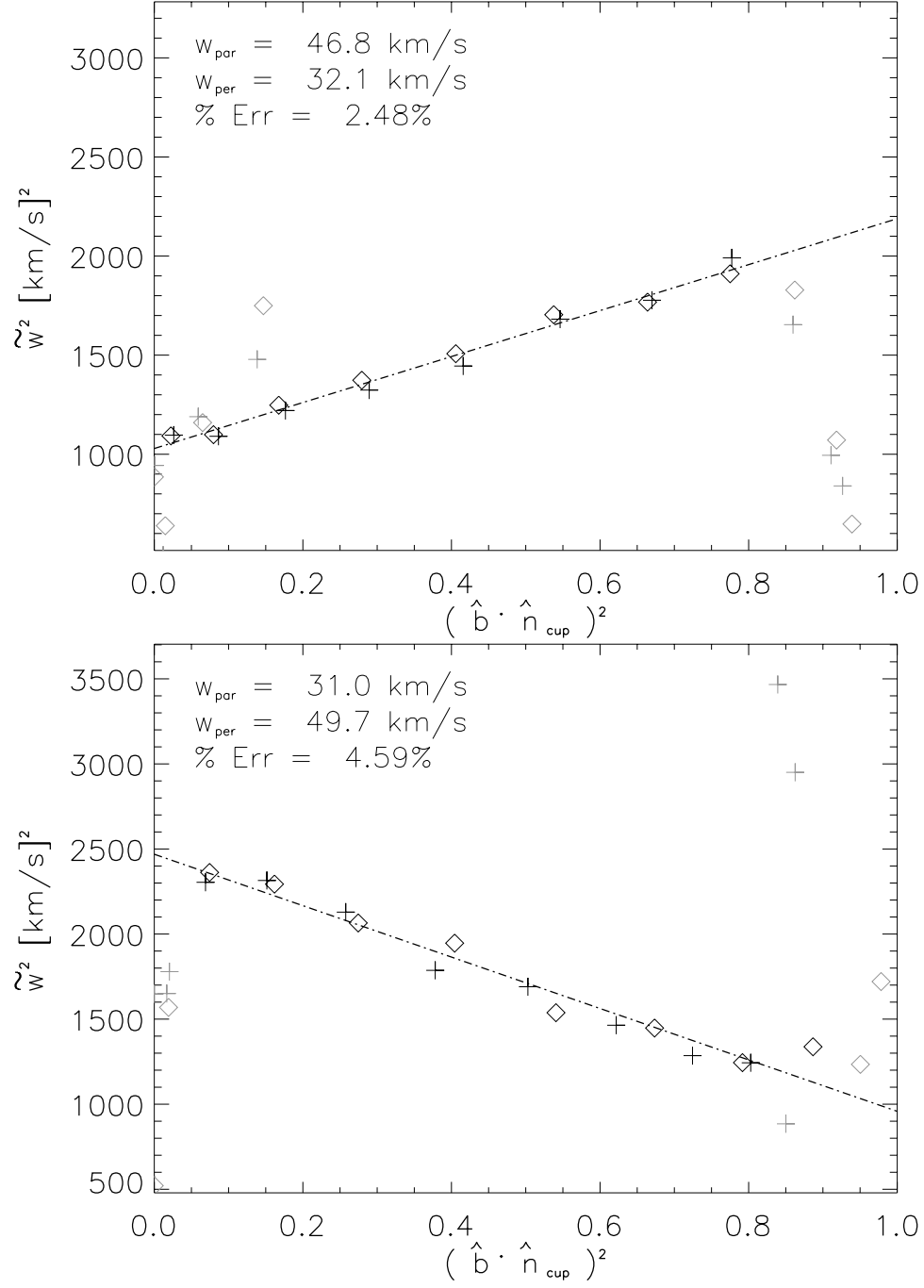


Figure 2-9: Scatter plot of observed thermal speed  $w(\hat{n})$  as a function of FC direction relative to the field orientation  $\hat{n}$ . Grey symbols indicate points discarded due to suspicious densities. The lines are the best fit of (2.24) to the selected observations. The data in the top panel are for the same spectrum shown in Figure 2-8 and have  $w_{\parallel} > w_{\perp}$ , whereas in the bottom panel  $w_{\parallel} < w_{\perp}$ .

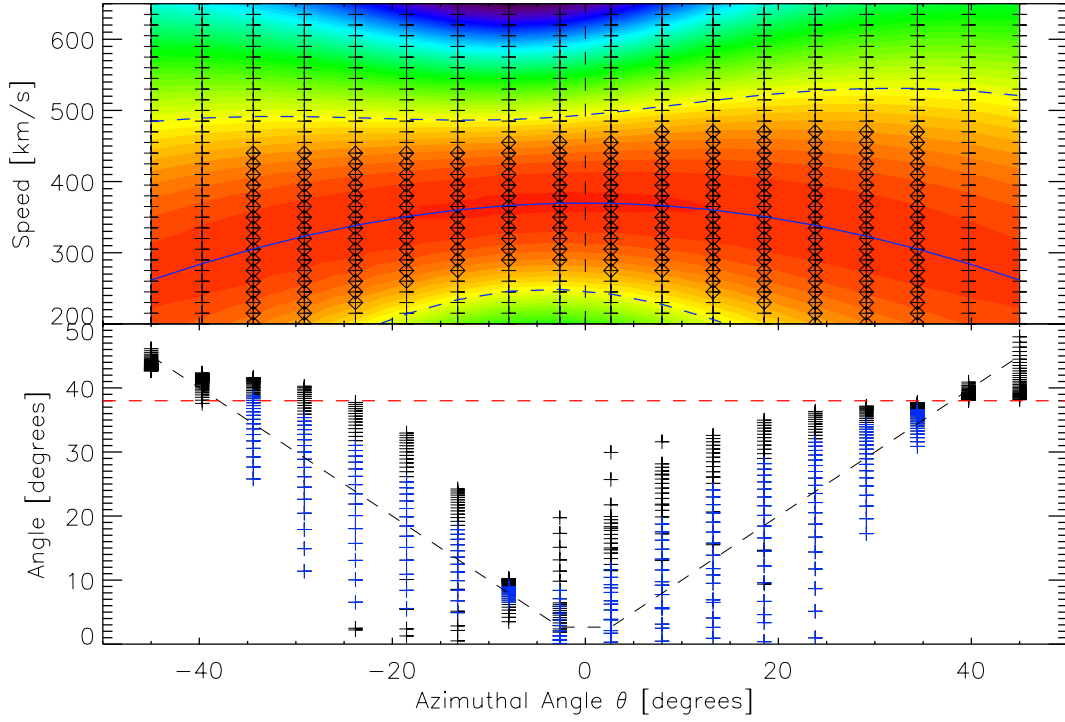


Figure 2-10: Selecting measurements of anisotropic proton distribution for fitting to bi-Maxwellian model. *Top panel:* Color shading indicates logarithmic distribution of observed current as a function of speed window and azimuthal angle; crosses are locations of measurements and diamonds are the selected points; solid line is projection of bulk velocity along each angle and dashed lines mark three thermal widths above and below this projection. *Bottom panel:* Crosses indicates the angle of incidence of the maximum flow for each measurement; Dashed horizontal line (red) is the maximum angle **ANGLEMAX** for selection; Dashed curve is the angle between the cup and the bulk flow; colored (blue) crosses are selected data.

Model/instrumental effects are due to properties of the Faraday Cups which are either not included in the derived models or limit the observations. Due to thermal fluctuations in the amplification electronics there is a background current of approximately  $2 \cdot 10^{-13}$  A that the proton flux must exceed to be detected. In addition, an intermittent increase in the background current along a single angle has been observed in the past. It is small compared to ion signatures and has the same value at each energy window along the single angle. The particular angle effected is also seen to change with time, leading us to believe that sunlight is glinting off an object on the spacecraft. Both of these effects are avoided by setting a minimum current **CURRMIN** which observations must exceed.

The final issue is due to the effects of ions at large angles of incidence to the cup. Several of the derivations fail for large angles of incidence: The initial assumptions listed in Section 2.2.3 for deriving the response functions required that the protons were supersonic and entirely in the field-of-view of the cup, thus allowing us to extend the integration in velocity space to an infinite slab; The derivation in Section 2.2.5 of the appropriate effective area was based on the assumption that the protons which contribute most to the measured current flow from an angle where the effective area varies slowly. In addition, at large angles the beam of particles which pass through the limiting aperture and illuminate the collecting plates may in part miss the collectors. As the modulator voltages alternates between the two edges of the window, the beam will partly walk on and off the collectors. This creates an artificial signal which is modulated at 200 Hz and is included in the final measured current. This feature is most often seen at very low voltages and large angles. Data which may experience any of these problems are discarded by setting a maximum angle **ANGLEMAX** to the cup normal. This limit is applied both to the angle between the cup normal and the bulk velocity and to the angle determined by (2.31) for the optimum effective area.

The main aspects of the point selection algorithm are illustrated in Figure 2-10 for a model proton spectrum. The proton VDF is bi-Maxwellian, flowing radially at  $-350$  km/s with  $\hat{b}$  in the ecliptic,  $-7^\circ$  from the Sun-Earth line and  $w_\perp = 2w_\parallel$ . The color shading is the logarithm of the observed current as a function of speed window and the azimuth angle of the cup. The crosses mark the location of every measurement in this spectrum and the diamonds are the selected observations. The solid blue line is the projection of the proton bulk speed as a function of the azimuth angle. The two dashed blue lines indicate the upper and lower speed limits with **THERMALMAX** set to 3. Note the variation in these bounds as a function of angle due to the varying effective thermal speed. The bottom panel shows the angle to the maximum flux as determined by (2.31) for each measurement as crosses. The dashed black curve is the angle between the cup and the bulk flow of the protons. The horizontal red dashed line is **ANGLEMAX**, which has been set to  $38^\circ$ . Selected points are colored blue.

A minimum of forty measurements of the proton distribution are required for the analysis to proceed on a given spectrum. Typically at least 200 points were selected.

### 2.3.5 Non-Linear Fit of Model to Observations

With the magnetic field orientation specified by the MFI field observations, there are six free parameters in the bi-Maxwellian proton model:  $\vec{U}$ ,  $w_{\perp}$ ,  $w_{\parallel}$ , and  $n$ . Define a  $\chi^2$  merit function,

$$\chi^2 = \sum_{i=1}^N \left[ \frac{I_i^{\text{meas}} - I_i^{\text{mod}}}{\sigma_i} \right]^2, \quad (2.43)$$

where for each measurement  $i$  of the total  $N$  observations there is an observed current  $I_i^{\text{meas}}$ , the current predicted by the model,  $I_i^{\text{mod}}$ , and the uncertainty  $\sigma_i$  of that measurement. The best-fit values of the parameters are determined by minimizing  $\chi^2$ . We employ the Levenberg-Marquardt non-linear least-squares method, which is a combination of the inverse-Hessian and steepest descent methods [Press et al., 1999, §15.5]. In addition to the best-fit parameters and the final minimum value of  $\chi^2$ , a covariance matrix is calculated and inverted to yield one- $\sigma$  estimates of the uncertainty of each parameter. The final value of  $\chi^2$ , combined with the number of measurements used in the fit, will indicate how well the bi-Maxwellian model describes solar wind protons.

If the Faraday Cup counted individual particles then the uncertainties  $\sigma_i$  in (2.43) would simply be proportional to the square root of the total number of particles detected. The uncertainty in the currents measured by the a FC is actually limited by the digitization of the observed currents as they are telemetered back to Earth. For the Wind cups the resolution of the telemetered currents is 1%. The weighting factor is set to the larger of one percent of the measured current or the thermal background current,

$$\sigma_i = (0.01 \cdot I_i^{\text{meas}} > 4 \cdot 10^{-13})^{-1}. \quad (2.44)$$

Note that the uncertainty of a Faraday Cup current measurement of  $N$  particles is not proportional to  $\sqrt{N}$ , but instead is fixed at  $0.01 \cdot N$ . It is not a great loss that the uncertainty due to the digitization is larger than simple  $\sqrt{N}$  statistics because the approximations we have used in deriving the instrument response introduce errors less than but near that same level.

## 2.4 Results: Proton Parameters, Uncertainty Propagation and Analysis

The original analysis code written to analyze Wind FC spectra was extended to incorporate the methods described in the previous section. The procedure is completely automated and processes a single day at a time, saving the results in a binary file. For each measurement the time, spacecraft location, magnetic field averages and fluctuations, results from the moment analysis, initial guess, best-fit parameters and their uncertainties, number of measurements selected for fitting, and the minimum value

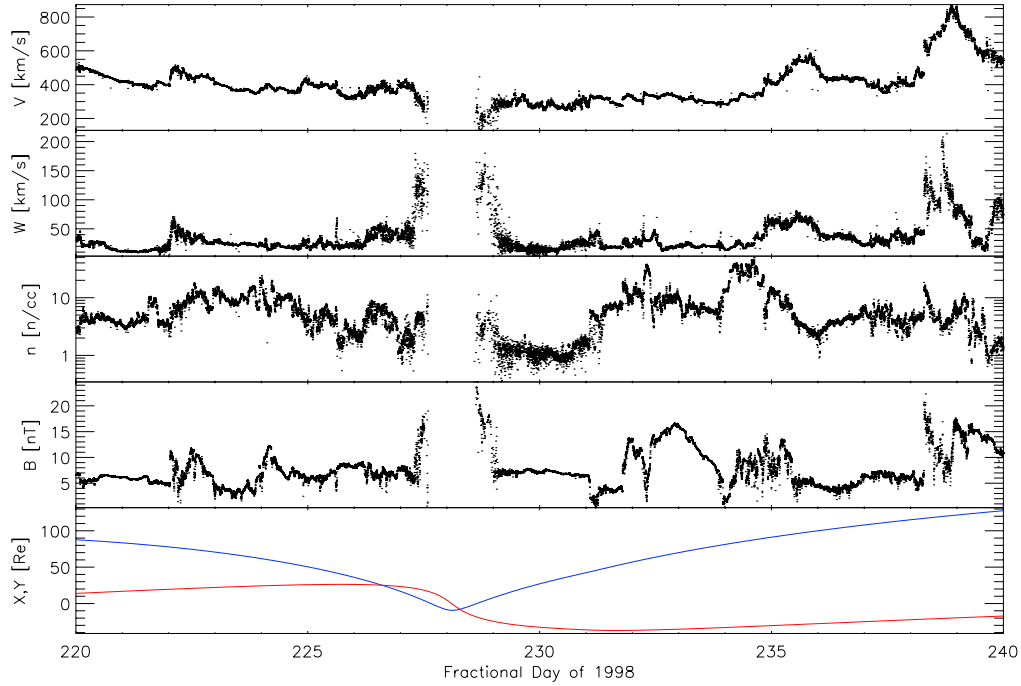


Figure 2-11: Selection of an interval in 1998 for the optimization of the analysis code. Shown from top to bottom are the bulk speed, thermal speed, number density, magnetic field, and location of the spacecraft ( $x_{\text{gse}}$  blue;  $y_{\text{gse}}$  red).

of  $\chi^2$  are recorded.

On average it takes ten minutes to analyze one day of observations, so our computer system can process the entire mission in approximately one week. Section 2.4.1 demonstrates how the small computing time allows us to optimize the data selection parameters which were described in Section 2.3.4.

The overall convergence of the non-linear analysis and the distribution of values of  $\chi^2$  are reviewed in Section 2.4.2. In the subsequent sections the uncertainties of the proton parameters are calculated, and any interesting dependencies are explored.

### 2.4.1 Optimizing the Analysis

In order to determine the best values for the two analysis parameters **THERMALMAX** and **ANGLEMAX** an interval of observations which cover a broad range of interplanetary conditions was selected and processed repeatedly. The “optimum” values of **THERMALMAX** and **ANGLEMAX** produce the best overall minimum average  $\chi^2/d.o.f.$  and anisotropic thermal speed uncertainties,  $\sigma_{w_{\perp}}$  and  $\sigma_{w_{\parallel}}$ .

Twenty days in 1998, from August 8 through August 28, containing 18,200 spectra, were selected for this procedure. A summary of the bulk speed, average thermal

Parameter	Value	Description
ANGLEMAX	28°	The maximum angle the bulk flow vector and the point in phase space making the greatest contribution to the current in this window may make
THERMALMAX	$3 \times \tilde{w}(\hat{b})$	Number of thermal widths from the peak using projected effective thermal speed at this angle
CURRMIN	$1 \times 10^{-12} [\text{A}]$	Minimum current
PEAKFRAC	$5 \times 10^{-3}$	Currents must be greater than this fraction of the peak current seen in the entire spectrum
ANGLEMOM	28°	Maximum angle from peak for moment analysis

Table 2.1: The final values of the free parameters used for the anisotropic analysis of protons.

speed, number density, magnetic field strength, and spacecraft location during this period is shown in Figure 2-11. The period was selected because it contained high and low speed solar wind, an encounter with the Earth’s bow shock, and several notable interplanetary shocks, especially the August 28 event.

The entire period of selected observations was processed four hundred times, using twenty values of THERMALMAX spaced evenly between 1.0 and 3.4, and twenty values of ANGLEMAX ranging from 10° to 50°. The median values for  $\chi^2/d.o.f.$ ,  $\sigma_{w\perp}$ , and  $\sigma_{w\parallel}$  were calculated. The dependence of  $\chi^2/d.o.f.$  and  $\sigma_{w\parallel}$  on the choice of THERMALMAX and ANGLEMAX are shown as contour plots in Figure 2-12. For ANGLEMAX less than 18° the model fit the selected observations very well, but the resulting parameters were erratic, suggesting that there was insufficient data to constrain the model successfully. Focusing on the contour of  $\chi^2/d.o.f.$ , there are two clear trends. First the median value of  $\chi^2/d.o.f.$  is a sharply decreasing function of THERMALMAX until approximately 2.5 thermal widths of data are selected. Second,  $\chi^2/d.o.f.$  reaches its minimum value for ANGLEMAX greater than about 25°, and decreases slowly afterwards. Examination of several individual events suggested that this slow decrease in  $\chi^2/d.o.f.$  was just due to adding more measurements which did not require the model to change a great deal. Recall that the model has 6 free parameters, while as ANGLEMAX increases in this range, the number of observations selected increases from  $\sim 150$  to upwards of  $\sim 250$  measurements. For the uncertainty in the thermal speed the best results came with ANGLEMAX greater than 25° and THERMALMAX greater than 2. The same results were seen in the median uncertainty in the perpendicular thermal speed. The slower variation of the results with THERMALMAX greater than 2.5 appears to be due to setting PEAKFRAC to 0.01, resulting in a limit to the number of measurements selected with increasing THERMALMAX.



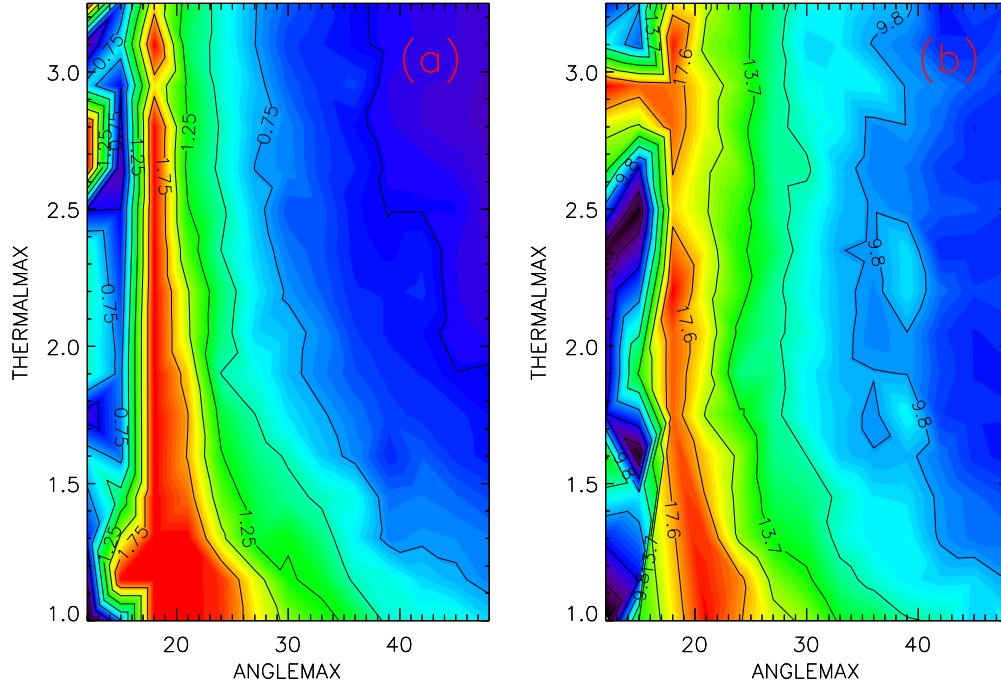


Figure 2-12: Two samples of the optimization procedure for selecting the values of **ANGLEMAX** and **THERMALMAX** which result in the best overall analysis. Panel (a) is the median value of  $\chi^2/\text{d.o.f.}$  and panel (b) is the median value of the percent uncertainty of the parallel thermal speed for each run over the 18,200 spectra contained in the selected interval.

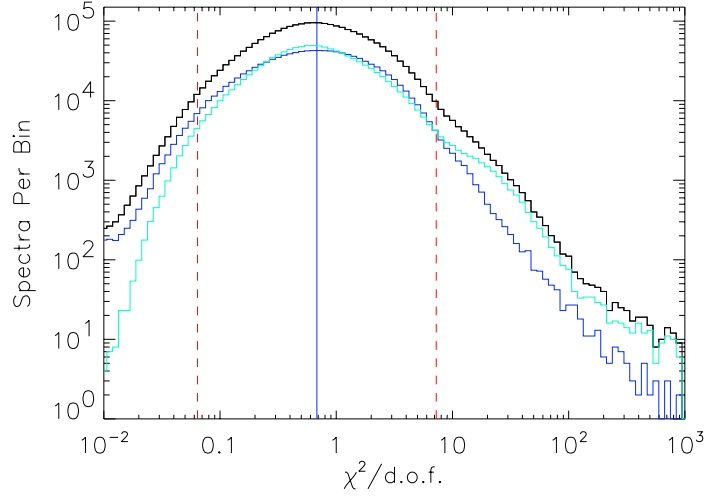


Figure 2-13: Distribution of the final value of  $\chi^2/\text{d.o.f.}$  for all spectra analyzed (black), slow solar wind  $v < 400$  km/s (green), fast solar wind  $v > 400$  km/s (blue). The average value of  $\chi^2/\text{d.o.f.}$  over all spectra was 0.68 (blue vertical line). The distribution of spectra is approximately log-normal, and 99.9% of the spectra, had final values of  $\chi^2/\text{d.o.f.}$  between 0.07 and 7.3 (red lines). It has approximately the same distribution

### 2.4.2 Overall Summary: Convergence, $\chi^2/\text{d.o.f.}$

To date the Faraday Cups have recorded 2,208,024 measurements, and this analysis produced a converging fit to 99.9957% of these spectra. The 95 spectra which were not fit all had measurements which were suggestive of some form of telemetry error, generally either one or more isolated currents at the maximum value of  $10^{-8}$  A measurable by the cups or empty observations containing no data. This is not to imply that the remaining fits were perfect, there are plenty of factors which come to mind that could cause trouble, such as low Mach numbers or large magnetic fluctuations. In the following sections we will examine the uncertainties in the derived parameters, but here we look at the values of  $\chi^2/\text{d.o.f.}$  as indicative of how well the bi-Maxwellian model describes solar wind proton velocity distributions.

The value of  $\chi^2$  may be used to identify how well the model describes the observations. For a system with  $\nu$  degrees of freedom the probability of measuring a value of up to  $\chi^2$  is given by [Abramowitz and Stegun, 1972, §6.5],

$$P(\chi^2|\nu) = \frac{1}{2^{\frac{1}{2}\nu}\Gamma(\frac{\nu}{2})} \int_0^{\chi^2} t^{\frac{1}{2}\nu-1} e^{-t/2} dt. \quad (2.45)$$

There are six parameters in the model, and if a total of  $N$  measurements were selected for fitting then there are  $\nu = N - 6$  degrees of freedom in the fit. The distribution of

the  $\chi^2/\nu$  for all solar wind observations and separately for the slow and fast solar wind are shown in Figure 2-13. The average value of  $\chi^2/\nu$  is slightly less than unity, and 99.9% of the observations had values of  $\chi^2/\nu \leq 7.3$ . To evaluate what this distribution tells us about the quality of the fits, (2.45) was evaluated individually for each spectrum. If the model described the data perfectly, then 50% of the time  $P(\chi^2|\nu)$  would be greater than 0.5 and 50% of the time it would be less than 0.5. The result of the calculation was 59% of the observations had  $P(\chi^2|\nu) < 0.5$ , 41% had  $P(\chi^2|\nu) > 0.5$ , which is close to the ideal values. It is expected that more of the spectra produced smaller values of  $\chi^2/\nu$  because of the nature of the uncertainty in the current being driven by the quantization of the signal and not the actual (and smaller) error due to counting statistics. It should be noted that the values of  $\chi^2/\nu$  recorded are an indication of how well the bi-Maxwellian model described the selected observations and not of how well or how completely the solar wind consists of anisotropic protons.

### 2.4.3 Bulk Speed, Velocity Components, and Flow Angles

Once the best-fit values of the solar wind parameters have been determined, the bulk velocity of the protons in the spacecraft frame is corrected for the 30 km/s aberration produced by the orbital velocity of the spacecraft and Earth around the Sun. Since the  $\hat{y}_{\text{GSE}}$  axis is anti-parallel to the direction of Earth's motion, this is done by subtracting 30 km/s from the  $\hat{y}_{\text{GSE}}$  component. I then took the individual uncertainties in the components of the velocity and calculated the propagated uncertainty in the bulk speed of the protons,

$$\sigma_U^2 = \Sigma_{i=x,y,z} \sigma_{U_i}^2 \left( \frac{\partial U}{\partial U_i} \right)^2 = \frac{\sigma_{U_x}^2 U_x^2 + \sigma_{U_y}^2 U_y^2 + \sigma_{U_z}^2 U_z^2}{U^2}. \quad (2.46)$$

We also use the components of the velocity to calculate the flow angles of the solar wind, traditionally defined at MIT as the direction *from which* the plasma is flowing. We calculate the East-West flow angle in the ecliptic plane,

$$\theta_{\text{EW}} = \tan^{-1} \frac{U_y}{U_x}, \quad (2.47)$$

and its uncertainty,

$$\sigma_{\text{EW}}^2 = \Sigma_{i=x,y} \sigma_{U_i}^2 \left( \frac{\partial \theta_{\text{EW}}}{\partial U_i} \right)^2 = \frac{U_x^2 \sigma_{U_x}^2 + U_y^2 \sigma_{U_y}^2}{(U_x^2 + U_y^2)^2}, \quad (2.48)$$

and the North-South flow angle out of the plane of the ecliptic,

$$\theta_{\text{NS}} = \tan^{-1} \frac{U_z}{\sqrt{U_x^2 + U_y^2}}, \quad (2.49)$$

and its uncertainty,

$$\sigma_{\text{NS}}^2 = \sum_{i=x,y,z} \sigma_{U_i}^2 \left( \frac{\partial \theta_{\text{NS}}}{\partial U_i} \right)^2 = \frac{(U_x^2 + U_y^2)^2 \sigma_{U_z}^2 + (U_x^2 \sigma_{U_x}^2 + U_y^2 \sigma_{U_y}^2) U_z^2}{(U_x^2 + U_y^2) U^4} \quad (2.50)$$

#### 2.4.4 Thermal Speeds

There are two possible issues that would prevent an accurate determination of  $w_{\perp}$  and  $w_{\parallel}$  which should be examined in detail: (1) if there is a large angular fluctuation of the magnetic field direction during the 92-second plasma spectrum I would expect any anisotropies in the thermal speed to “wash out”; (2) certain orientations of the magnetic field, even if it is steady, could make it difficult to determine one or both of the thermal speeds.

To address fluctuations, I looked at the ratio of the thermal speeds under two cases: spectra recorded with a large fluctuation of the magnitude of the field but little change in the direction of the field, and the opposite, cases where the magnitude of the field did not change much, but there was a large angular fluctuation. The results are shown in Figure 2-14. It is clear that while changes in the magnitude of the field do not appear to change the distribution of thermal speed ratios, there is a dramatic drop in anisotropy when the angular fluctuation of the magnetic field exceeds  $x$  degrees. For subsequent analysis of temperature anisotropies therefore I will restrict myself to cases where the angular fluctuation is less than  $20^\circ$  (this choice leaves 96% of the total spectra). It is worth asking if a plasma undergoing significant angular fluctuation of the magnetic field orientation over the course of the 92-second recording time of a Faraday Cup spectra actually becomes isotropic. One expects high frequency oscillations on the order of the ion cyclotron frequency to efficiently couple to the ion distribution function, so that under the influence of fluctuations on the order of minutes one would expect the field to remain frozen in to the plasma, and for little mixing of the thermal speeds to occur. A future investigation might pursue fitting the wind observations with  $\tilde{w}(\hat{b}(t))$ , using the fastest possible magnetic field data, preferably the 40 millisecond measurements, and checking to see if that produces a better fit. A detailed study of the quality of the fit as a function of the frequency of the fluctuations might provide insight into the exact mechanisms by which the electromagnetic fluctuations are coupling to the particle distributions.

To explore the uncertainties in the thermal speeds, plots of the median uncertainty of  $w_{\perp}$  and  $w_{\parallel}$  as a function of magnetic field latitude,  $\theta_B$ ,

$$\theta_B \equiv \tan^{-1} \frac{B_z}{\sqrt{B_x^2 + B_y^2}}, \quad (2.51)$$

and magnetic longitude,

$$\phi_B \equiv \tan^{-1} \frac{B_y}{B_x}, \quad (2.52)$$

were generated for each parameter. The magnetic field typically lies in the plane of

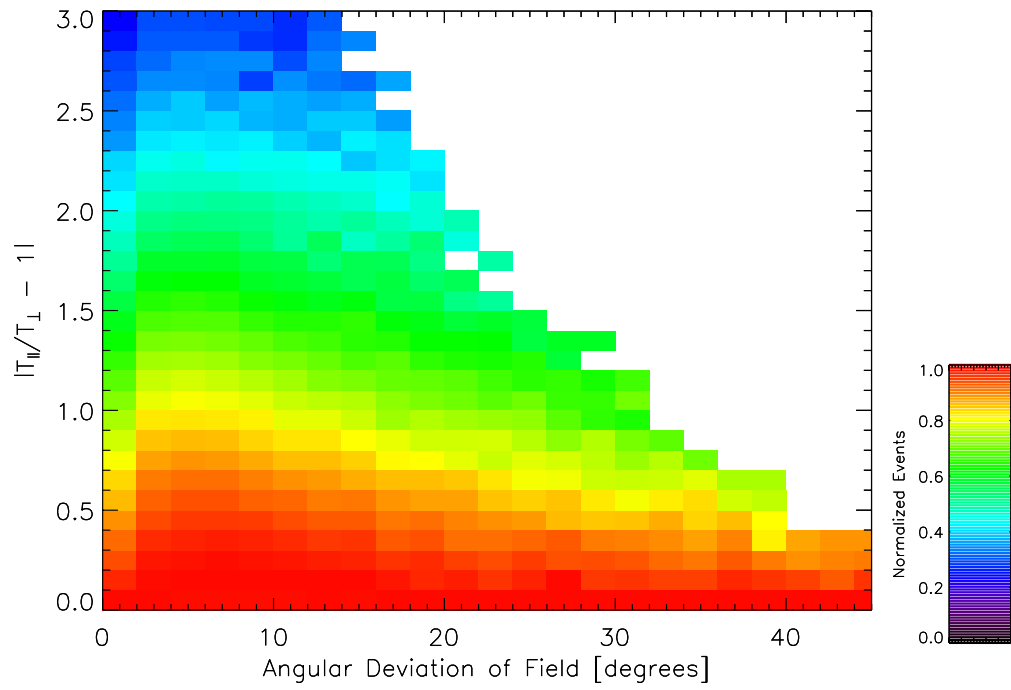


Figure 2-14: Testing the effect of angular field fluctuations during recording of ion spectrum. This is a plot of the temperature anisotropy as a function of the angular deviation of the field, as defined by equation (2.42).

the ecliptic along the Parker spiral angle of about  $45^\circ$ . Therefore the  $(\theta_B, \phi_B)$  plane is not evenly covered by the observations.

A summary of the agreement between the moments and the non-linear analysis was presented by Tanabe et al. [2001]. In general the two techniques produced results which agreed to within 30%. The largest differences occurred near interplanetary shocks and in very high speed solar wind.

To determine if the average disagreements between moment and non-linear analysis techniques are instrumental or physical the observed discrepancy is compared to Monte-Carlo simulations of solar wind ion spectra. For each given value of  $w_{\parallel}$ , 50000 solar wind parameters were generated randomly and the Faraday Cup response was determined using the non-linear bi-Maxwellian response function. This response was then fed into the anisotropic moment analysis code and the results were compared. The diamonds are the observed differences from Figure 2.4.4, the blue lines are the result of the first simulation (thick line is average value of ratio, thin lines mark on standard deviation from mean). Result are reproduced well for  $w_{\parallel} \geq 90$  but the simulation does not predict the large errors at smaller values of  $w_{\parallel}$ . The simulation was improved by including a distribution of alpha particles, resulting in the red curves, which provide a much better agreement with observations. It seems clear that on average the  $\sim 20\%$  differences between thermal speeds determined by moment and non-linear analysis techniques are due to a breakdown of the moment method, through contamination by alpha particles and loss of part of the distribution in the case of hot spectra.

For the thermal speeds we would also like to produce an equivalent thermal speed. Starting with the idea of forming a single pressure from an isotropic pressure tensor  $\mathbf{P}$  by taking the trace,

$$P_{\text{iso}} \equiv \text{Trace}(\mathbf{P})/3, \quad (2.53)$$

then there is an equivalent relation for the temperatures,

$$T_{\text{iso}} \equiv \text{Trace}(\mathbf{T})/3 = 2T_{\perp} + T_{\parallel}, \quad (2.54)$$

where we have assumed we are dealing with a gyrotropic bi-Maxwellian distribution function. Since  $T_{\perp} = \frac{1}{2}m_p w_{\perp}^2$ ,  $T_{\parallel} = \frac{1}{2}m_p w_{\parallel}^2$ , we can then write down a relation for the isotropic thermal speed  $w_{\text{iso}}$ ,

$$w_{\text{iso}} \equiv \sqrt{(2w_{\perp}^2 + w_{\parallel}^2)/3}, \quad (2.55)$$

and its associated propagated uncertainty,

$$\sigma_{w_{\text{iso}}}^2 = \frac{w_{\parallel}^2 \sigma_{w_{\parallel}}^2 + 4w_{\perp}^2 \sigma_{w_{\perp}}^2}{3w_{\parallel}^2 + 6w_{\perp}^2}. \quad (2.56)$$

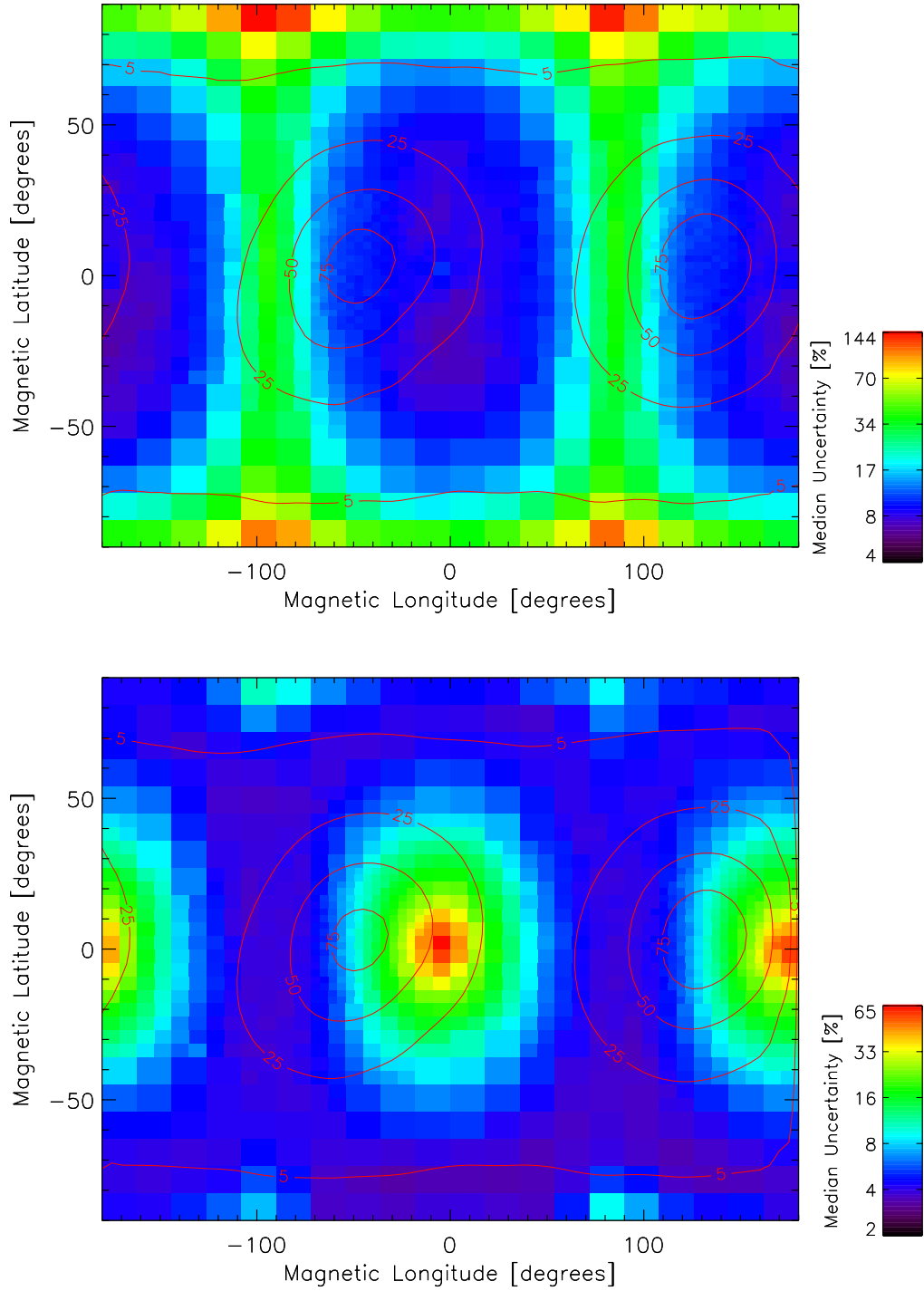


Figure 2-15: Dependence of the uncertainty in parallel (upper panel) and perpendicular (lower panel) proton thermal speeds as a function of magnetic latitude and longitude. Color shading indicates median uncertainty as indicated by color bars on left. Red curves indicate 5,25,50,75% measurement contours. See text for details.

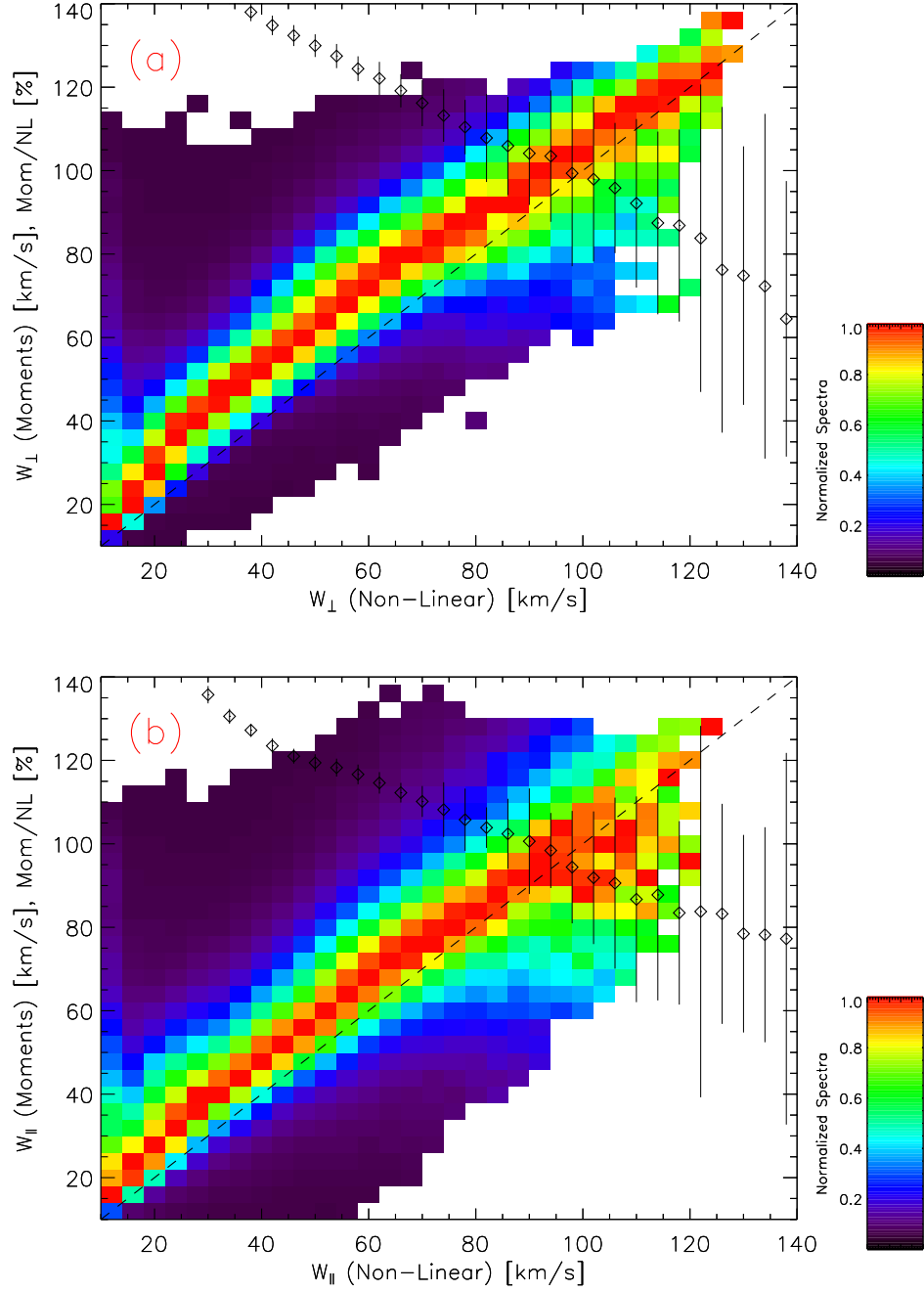


Figure 2-16: Comparison of the thermal speeds as determined by the non-linear and moment analysis techniques. Colored bins indicate the number of spectra in a two-dimensional histogram. Each column has been normalized to unity. Dashed line indicates equality between methods; diamonds are the average ratio between the methods (in percent) as a function of the non-linear value, with error bars indicating the deviation of the ratio in each bin.



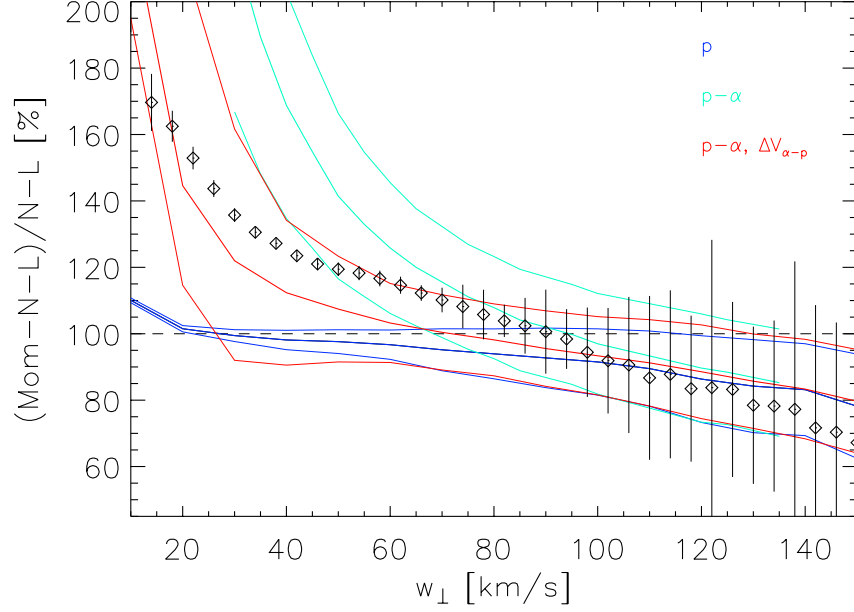


Figure 2-17: Comparison of moment and non-linear anisotropies with the predictions of numerical Monte-Carlo simulations.

### 2.4.5 Number Density

The average uncertainty in the proton number density over all spectra was  $x \pm y\%$ , with a median value of  $x\%$ . The two parameters this uncertainty is most dependent on are the bulk speed of the protons,  $U_p$ , and the thermal width of the proton distribution, where for simplicity here I will overlook any temperature anisotropies by using the single isotropic thermal speed,  $w_{\text{iso}}$  defined by (2.55).

To get a good idea of the percent uncertainty in the number density,

$$100\% \times \frac{\sigma_{n_p}}{n_p}, \quad (2.57)$$

due to the instrument response as a function of  $U_p$  and  $w_{\text{iso}}$ , we generated the plot shown in Figure 2-18.

It is most dependent on the thermal speed and the bulk speed, so I generated a two-dimensional plot of the average percent uncertainty of the number density as a function of the proton bulk speed and the isotropic thermal speed (2.55). I initially divided the plot into 20 intervals spaced logarithmically in number density and linearly spaced in thermal speed. Then I looked at each interval and if there were more than 50 points in that bin I subdivided the bin into quarters. This procedure results in a two-dimensional visualization of the dependence of the thermal speed, with higher resolution in areas with more data.

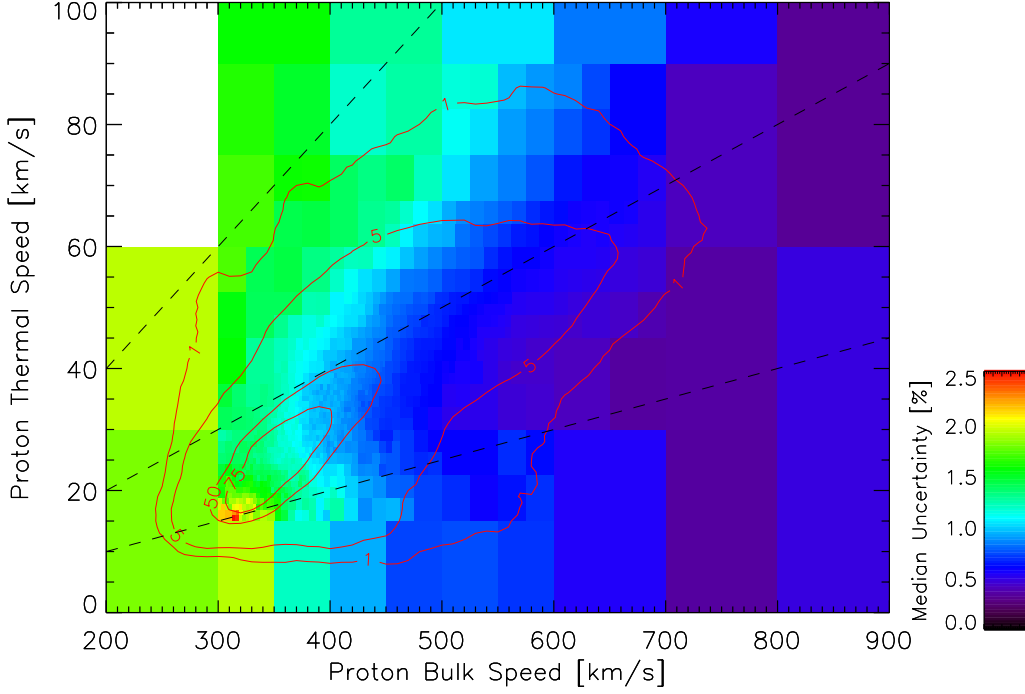


Figure 2-18: The median uncertainty in proton number density as a function of the bulk speed and the calculated isotropic thermal speed. Each bin contains at least 1,000 spectra; and, where the density of measurements permitted, the resolution of the bins has been increased. The four red contours mark the boundaries at which the density of measurements has fallen to 1, 5, 50, and 75% of the maximum value. Dashed black lines indicate thermal to bulk speed ratios of 5, 10, and 20.

Parameter	Units	Mean	Median	Stdev	Mean %	Median %
$ U $	km/s	13.5	10.1	10.8	3.1	2.6
$U_x$	km/s	13.6	10.1	10.9	3.1	2.7
$U_y$	km/s	1.8	1.0	2.9	12.2	10.5
$U_z$	km/s	1.7	0.9	2.5	10.7	9.2
$\theta_{EW}$	degree	0.03	0.03	0.02	N/A	N/A
$\theta_{NS}$	degree	0.04	0.03	0.01	N/A	N/A
$w_{\perp}$	km/s	2.6	1.3	4.0	7.7	4.9
$w_{\parallel}$	km/s	6.0	3.3	7.8	15.5	10.7
$n_p$	$\text{cm}^{-3}$	0.2	0.1	0.4	1.4	1.2

Table 2.2: Uncertainties in each of the derived parameters from the best-fit to individual solar wind spectra.

## 2.5 Summary

The response of the Faraday Cup instruments on Wind to a convected, bi-Maxwellian distribution of ions has been derived and applied to the observations for the first time. Faraday Cups are the only thermal plasma instruments for which analytical response functions have been derived. Therefore while other investigations in the past have determined ion plasma parameters including temperature anisotropies, this is the first analysis which produced uncertainty estimates for each of the derived parameters along with the  $\chi^2/d.o.f.$  estimate of the quality of the fit. Indeed the dataset submitted to the NSSDC, which includes these uncertainties for each spectrum, is the first of its kind. It has been shown that the typical uncertainties of the proton solar wind parameters determined by the FC instruments are all on the order of a few percent, that the average  $\chi^2/d.o.f.$  near unity implies that bi-Maxwellian distributions are a good description of the solar wind ions at 1 A.U., and that differences between the moment and non-linear analysis techniques are predominantly due to failures in the approximations which go into the moments.

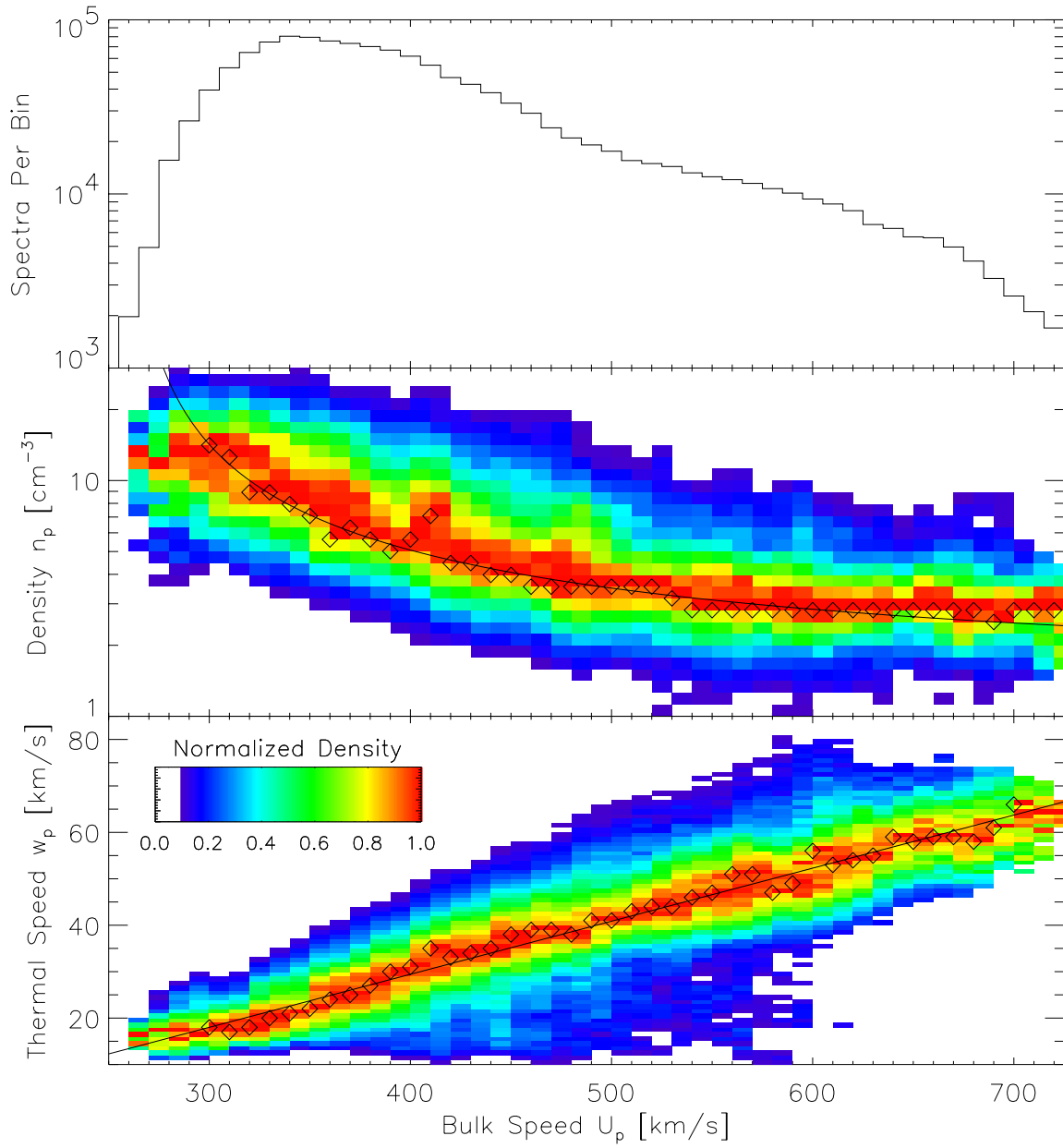


Figure 2-19: Survey of proton parameters in the solar wind at 1 AU as seen by the Wind Faraday Cup instruments. *Upper panel:* The distribution of proton number densities  $n_p$  as a function of bulk speeds  $U_p$ , showing that on average the particle flux  $n_p U_p$  is conserved. *Lower panel:* Single proton temperature  $T_p = (2T_{p\perp} + T_{p\parallel})/3$  as a function of bulk speed, showing that on average the solar wind has a mach number  $U_p/w_p \sim 10$ .

# Chapter 4

## Extension of Analysis to Helium

**ABSTRACT:** *The bi-Maxwellian analysis techniques developed in Chapter 2 to characterize Faraday Cup observations of protons are extended to alpha particles. The success of this procedure is reported, and the results are used to compare Faraday Cup densities with WAVES/TNR observations of the electron plasma frequency.*

### 4.1 Ion Composition of the Solar Wind

Protons are not the only constituent of the ion component of the solar wind. Fully ionized helium or alpha particles generally account for 1% – 5%, and sometimes as much as 10%, of the ions by number density. Minor ions such as oxygen and iron make up an additional 1%. The properties of these additional ion species contain a great deal of information which is useful for a variety of applications. Broadly speaking the details of the additional ion species are interesting because they effect the dynamics of the interplanetary medium, reflect the origin and acceleration mechanisms of the solar wind, and exhibit the effects of a range of kinetic plasma micro-instabilities.

The Faraday Cup (FC) ion instruments on the Wind spacecraft were introduced in Chapter 2, along with the derivation and application of the convected, field-aligned, bi-Maxwellian velocity distribution function (VDF). As a result of that analysis a best-fit to each ion spectrum yielded a set of proton parameters  $\vec{U}_p, T_{\perp p}, T_{\parallel p}, n_p$ , their uncertainties, and the  $\chi^2/\nu$  parameter. This chapter describes the extension of that analysis to produce, when possible, the same set of bulk parameters for the alpha particles,  $\vec{U}_\alpha, T_{\perp \alpha}, T_{\parallel \alpha}, n_\alpha$ . Scientific applications of the alpha measurements are considered in the following chapter.

The additional procedures created to analyze the helium in addition to the protons are described in Section 4.2. Section 4.3 details the results of this analysis, including the success rates. In Section 4.4 the proton and alpha number densities are used in conjunction with the WAVES experiment on Wind to conduct a study of the absolute calibration of the Wind Faraday Cups. In order to continue treating the solar wind as a fluid in the presence of multiple ion species a single fluid description must be developed, and this is done in Section 4.5. A brief summary following in Section 4.6.

## 4.2 Extension of the Existing Analysis Code

The analysis code was extended to include fitting of the alpha measurements using the methods developed by Aellig as a starting point [Aellig et al., 2001b]. Since the alphas often partially overlap with the protons it was decided that the moment analysis was too susceptible to contamination by hydrogen, so only the non-linear analysis is applied to the helium component of the measurements. No additional work is needed to produce the alpha particle response function. The derivation of the convected bi-Maxwellian response in Section 2.2.4 is used for the alphas, just with the substitution of with charge  $2q$  and mass  $4m_p$ .

The additional program starts after the existing code has successfully produced a converging fit to the proton VDF. If the proton fit was successful then the spectrum is assigned a fit status of 11, if it failed then the fit status is 0 and the code proceeds with the next spectrum. An initial guess is made that the alpha particles have the same parameters as the protons, except with  $n_\alpha/n_p = 5\%$ , which is a typical value in the solar wind. An extension of the data selection algorithm described in Section 2.3.4 then identifies measurements in the spectrum which are expected to correspond to either protons or alphas. At least 10 points from each cup corresponding to alphas must be selected for the analysis to proceed. The selected data, typically 300-400 measurements, are then subjected to a simultaneous fit with twelve free parameters,  $\vec{U}_p, w_{\perp p}, w_{\parallel p}, n_p, \vec{U}_\alpha, w_{\perp \alpha}, w_{\parallel \alpha}$ , and  $n_\alpha$ .

An single isotropic thermal speed for each species is then calculated,  $w_j^2 = (2w_{\perp j}^2 + w_{\parallel j}^2)/3$ . In Section 5.3 it will be shown that in general  $T_\alpha = T_p$  or  $T_\alpha = 4T_\perp$ . This is because ion species in the solar wind are generally either in thermal equilibrium, in which case  $w_\alpha = w_p/2$ , or have equal thermal speeds. If  $w_\alpha/w_p \leq 0.75$  then the spectrum is assigned a fit status of 8. No further action is taken but the spectrum is flagged for future investigation as a period where the alphas are cold. If  $w_\alpha/w_p \geq 2.2$  then there is the possibility that the alpha and proton distributions overlap and as a result the alpha temperature is too high. In this case fit status is 9 and the analysis will re-perform the alpha fit after subtracting the best fit to the proton distribution.

If  $U_\alpha/U_p \geq 1.1$  then the spectrum is assigned a fit status of 7. No further action is taken but the measurements might be useful in studies of intervals with fast alpha particles. If  $U_\alpha/U_p \leq 0.97$  or  $n_\alpha/n_p \geq 20\%$  then there is the danger that a double streaming proton distribution has been accidentally fit as the alpha distribution. In this case the proton fit is subtracted and the alpha distribution is fit to the remaining data.

If after subtraction of the proton data the alpha parameters seem reasonable then the spectrum is assigned a fit status of 5. If after subtraction the parameters are still suspicious then the final fit status is 4 if the alphas are too cold, 3 if they seem too hot, and 2 if they appear too slow. If there are multiple problems with a spectrum it is assigned a fit status of zero.

The final results are the same as described in Section 2.4, just with the addition of the alpha parameters and the fit status. For each spectrum the best-fit parameters,  $\vec{U}_p, w_{\perp p}, w_{\parallel p}, n_p, \vec{U}_\alpha, w_{\perp \alpha}, w_{\parallel \alpha}$ , and  $n_\alpha$ , estimates of their one-sigma uncertainties, the number of measurements selected in each cup, the final value of  $\chi^2/\nu$ , and an array

Fit Status	All	Solar wind	Fast SW $V_p > 400$	Slow SW $V_p < 400$	MSH
0	1.71	1.35	1.42	1.30	14.02
1	16.46	16.06	16.34	15.67	31.41
2	12.66	12.70	15.31	10.08	11.40
3	10.92	11.15	15.37	6.89	2.81
4	0.01	0.01	0.01	0.03	0.00
5	2.43	2.49	2.18	2.82	0.63
6	1.36	1.37	1.40	1.36	0.92
7	3.00	2.58	4.64	0.49	14.76
8	0.08	0.08	0.03	0.14	0.00
9	0.99	1.01	0.44	1.60	0.45
10	48.41	49.45	40.98	58.06	16.45
11	1.92	1.68	1.87	1.47	7.08
Total spectra	2,351,008	2,257,338	1,135,940	1,120,949	57,344

Table 4.1: The success rate of the alpha-proton analysis procedure in various regions in space as a function of the final status of the fit.

of diagnostic parameters are saved to file.

### 4.3 Results of the Analysis

As of summer 2002 the bi-Maxwellian alpha-proton analysis procedure has been run on more than 2.3 million Faraday Cup spectra. The success of the analysis is illuminated by the statistics in Table 4.1, which break down the percentage of ion spectra as a function of final fit status. The percentage distribution is broken down into several regimes in the solar wind, including all observations, all solar wind observations, and intervals in the fast solar wind ( $U_p \geq 400$  km/s), slow solar wind ( $U_p \leq 400$  km/s), and magnetosheath intervals. In general there was insufficient data to characterize the alpha distribution 1.9% of the time, based on the number of spectra with a fit status of 11. This was a much larger problem in the magnetosheath, where it occurred 7% of the time. The greatest obstacle to characterizing the alpha particles with a Faraday Cup spectrum is when the proton temperature is especially high, and this is a frequent occurrence in the magnetosheath.

A perfect fit status of 10 occurred 58% of the time in the slow solar wind, and 40% of the time in the fast wind. This can be attributed to three factors. First, as will be discussed in the following chapter, more collisions have occurred in slow solar wind as it propagates from the corona, due to the higher densities and slower travel speeds. As a result the alpha and proton velocities and temperatures tend to be in better agreement as the wind has settled into a more classical definition of equilibrium. Additionally, double streaming protons are a very common feature of the

Parameter	Units	Mean	Median	Stdev	Mean %	Median %
$ U $	km/s	57.7	44.7	43.7	14.1	11.9
$U_x$	km/s	57.8	44.8	43.8	14.2	11.9
$U_y$	km/s	6.0	3.7	7.5	45.6	42.3
$U_z$	km/s	5.4	3.3	6.5	42.2	38.3
$\theta_{\text{EW}}$	degree	0.18	0.13	0.33	N/A	N/A
$\theta_{\text{NS}}$	degree	0.24	0.01	0.17	N/A	N/A
$w_{\perp}$	km/s	10.2	5.7	11.4	32.7	27.1
$w_{\parallel}$	km/s	13.9	8.9	13.8	45.9	43.1
$n_{\alpha}$	$\text{cm}^{-3}$	$4 \cdot 10^{-4}$	$2 \cdot 10^{-4}$	0.003	0.12	0.11

Table 4.2: Uncertainties in each of the derived alpha parameters from the best-fit to individual solar wind spectra. Compare with same table for proton parameters in Table 2.2.

high speed solar wind [Clack et al., 2002]. Finally, at high speeds the alpha particle VDF is sometimes not completely observed by the Faraday Cups in their standard speed windows. As a result the fits to the alpha particles at very high speeds do not succeed as often.

## 4.4 Absolute Calibration of Number Densities

The analysis of Wind Faraday Cup ion spectra in Chapters 2 and 4 have established the accuracy with which we can measure proton and alpha particle number densities in the solar wind. The survey in Section 2.4.5 demonstrated how the one-sigma estimates of the uncertainties from the non-linear fits yielded averages values of  $\sigma_{np}/n_p \sim 0.5\%$  and  $\sigma_{n\alpha}/n_{\alpha} \sim 1\%$  over a broad range of solar wind conditions. This is the accuracy with which the convected bi-Maxwellian response function derived in Section 2.2 and applied to the observations can determine the number densities. In this section we will examine the the *precision*, or absolute uncertainty, of these measurements.

Traditional tests of the precision of bulk solar wind parameters involve the comparison of observations by different instruments on the same spacecraft, of observations from multiple spacecraft. Of course this comparison introduces additional uncertainties. Each instrument has its own sensitivities, and each investigator has a preferred analysis methodology which can result in systematic discrepancies. Recall the comparison in Section 2.4.4 of proton thermal speeds using data from the *same* Faraday Cup but with the application of the moment and non-linear techniques. Additionally factors such as differing measurement cadences must also be taken into account. Multi-spacecraft comparisons suffer from the spacecraft separation and the intrinsic temporal and spatial variation of the solar wind. It has been known for some time that there are correlation lengthscales in the interplanetary medium which are in general are also of the order of typical spacecraft separations [Jurac and Richardson, 2001].



Additionally, recent studies have shown that the boundaries between structures in the solar wind, while often planar on the length-scale of spacecraft separations, are in general not radial [Weimer et al., 2002]. Thus it is not a simple procedure to propagate observations from one spacecraft to another.

This study makes use of another instrument on the same spacecraft which measures the total electron number density in a completely independent manner. The Thermal Noise Receiver (TNR) instrument in the WAVES experiment measures the power of electromagnetic fluctuations at a very high cadence of 0.2-4.5 seconds in the frequency range from 4 – 300 KHz [Bougeret et al., 1995]. It was shown in Section 1.2.8 that the solar wind plasma fluctuates at the electron plasma frequency  $\omega_{p,e}$ , a quantity which is only a function of the total electron number density (1.92) and which varies from 50–300 KHz in typical solar wind conditions. Generally a single TNR power spectrum may be used to determine the electron number density using a neural network which identifies the peak of the plasma frequency line.

The goal of this section therefore is to compare a predicted value for the electron number density  $n_e$  based on the observed proton  $n_p$  and alpha  $n_\alpha$  number densities and compare with the TNR measurements. Since hydrogen and helium are fully ionized in the solar wind the total electron number density due to protons and alphas is  $n_p + 2n_\alpha$ . In order to do this correctly however we need to take into account the contribution of other ion species in the solar wind. Recall that  $\sim 1\%$  of the solar wind by number density is composed of minor ions like oxygen and iron. While these minor ions are rare the typical charge states observed are  $^{+7}\text{O}$  and  $^{+10}\text{Fe}$ , so a small abundance can result in a significant contribution to  $n_e$ . As was shown in Section 1.2.7, on the time scale of a FC measurement of the ion VDF there are no electric fields other than that due to the convection of the plasma and the solar wind is neutral. The requirement of charge neutrality may be written,

$$|q_e|n_e = \sum_j q_j n_j, \quad (4.1)$$

where  $q_j$  is the average charge state of the  $j^{\text{th}}$  species which has a number density  $n_j$ . If  $n_e$  is the total electron number density measured by TNR, and all of the measurements were exact, then the fraction  $F_m$  of  $n_e$  due to minor ions is,

$$F_m \equiv \frac{1}{n_e}(n_e - n_p - 2n_\alpha) = 1 - \frac{n_p}{n_e} - 2\frac{n_\alpha}{n_e}. \quad (4.2)$$

In reality each of the measurements which go into (4.2) have an uncertainty which we will label  $\sigma_p$ ,  $\sigma_\alpha$ , and  $\sigma_e$ . The propagated uncertainty in  $F_m$ , or  $\sigma_m$ , is then,

$$\sigma_m^2 = (n_p + 2n_\alpha)^2 \frac{\sigma_e^2}{n_e^2} + \frac{\sigma_p^2}{n_e^2} + \frac{\sigma_\alpha^2}{n_e^2}. \quad (4.3)$$

In this study we will look at the average value of  $F_m$  and its variation  $\Delta F_m$  as a function of the proton speed and the year of the mission. This is because many properties of the minor ions have been demonstrated to be speed and solar cycle

Component	Relative Abundance	Electrons	Similar Species	Total Electrons
Hydrogen	$10^3$	$10^3$	1	$10^3$
Helium	50	$2 \cdot 50$	1	100
Oxygen	1	$7 \cdot 1$	3	28
Iron	0.1	$10 \cdot 0.1$	6	7

Table 4.3: Estimating the contribution of minor ion species to the total electron content. With the numbers listed here  $F_m \simeq 3.1\%$ .

dependent. If the absolute calibrations of both the FC and TNR instruments are correct then  $F_m$  should agree with the results of other studies. Additionally, if all of the instrumental effects are correctly captured in  $\sigma_p$ ,  $\sigma_\alpha$ , and  $\sigma_e$ , then the quantity  $(\Delta F_m^2 - \sigma_e^2)^{1/2}$  is indicative of the natural variation of the minor ion component. It is a convolution of the variation in minor ion abundance and charge state distribution.

A comparison of SWE/FC and WAVES/TNR observations, limited to six days in 1996, was reported previously [Maksimovic et al., 1998, Figure 2]. In that study there was a general disagreement on the order of  $F_m \sim 1\%$  and a spread of approximately 5%. There are several compelling reasons to pursue this comparison in more detail. Significantly, the analysis of the TNR data have subsequently been refined due to a better understanding of the antennae and the TNR frequency bins. This has increased the observed values of  $F_m$ , but we hope to explain this by factoring in the effect of the minor ions. In addition, six days is insufficient to probe possible dependencies on solar wind conditions, such as the bulk speed. Finally, with our new knowledge of  $\sigma_p$  and  $\sigma_\alpha$  from the non-linear analysis we can separate the contributions of the protons, alphas, and minor ions to the observed 5% spread in  $F_m$ .

In preparation for this study we can estimate  $F_m$ . Table 4.3 lists values which are used in the following simple calculation [T. Zurbuchen, private communication]. The second column lists the relative abundances of each element, normalized to oxygen. Assuming that the hydrogen and helium are fully ionized, that oxygen and 3 more species like it are in a +7 charge state, and that iron and 6 species like it are in charge state +10, then

$$F_m \simeq 3.1\%. \quad (4.4)$$

Of course this is an approximation: There are other ions, and the charge states and relative abundances are highly variable. Predictions of  $F_m \sim 5\%$  were also discussed, and so the expected range in  $F_m$  is between 3% – 5%.

#### 4.4.1 Preparation of Measurements

This study uses all solar wind observations in the interval 1995-2000. Since the end goal is to produce as clear and confident a value for  $F_m$  as possible, any measurements

which seem at all suspicious are discarded. For the alpha particle analysis only spectra with a perfect final fit status of 10 (Section 4.2) are selected.

An infrequent issue with the high voltage power supply on FC1, the southward facing cup on Wind had to be addressed. On several occasions, especially early in the mission and during a 10-day interval in 1996, an error with the selection of energy windows for FC1 lead to incorrect density measurements. The standard key-parameter analysis code is designed to switch to a single-cup mode in the event of poor data quality from a single cup. Since the bi-Maxwellian analysis requires observations at as many angles relative to the ambient magnetic field as possible, it was decided that we would not conduct an anisotropy analysis during those intervals. To identify questionable spectra we ran the moment analysis code separately on the observations from each cup individually for each spectra and then compared the two determinations of the proton number density from each cup,  $n_{p1}$  and  $n_{p2}$ . The top panel of Figure 4-1 is a series of histograms of the density ratio  $n_{p1}/n_{p2}$  for each year from 1995-2000. The core of each histogram is a Gaussian with an average width of 2% and centers ranged between 99.1% and 100.2%. Statistically then the proton number densities in general determined independently by the two Faraday Cups using the moment analysis technique differ by 2%. The  $\pm 0.5\%$  range in the centers suggests that there is no bias in densities between the two cups. The result of the extended anomalous period in 1996 is clear in the top middle histogram in the form of the bulge on the  $n_{p1}/n_{p2}$  side. To be safe we will discard all measurements which do not satisfy  $0.9 \leq n_{p1}/n_{p2} \leq 1.1$ , or 0.18% of the total dataset.

The typical duration of a single SWE/FC ion spectrum is 92 seconds. The WAVES/TNR neural network data which were made available for this study are produced at a rate of at least one every 6 seconds. For the purposes of this study the TNR data were matched up to each FC spectrum and the average  $n_e$ , median, standard deviation  $\Delta n_e$ , and number of TNR measurements  $N$  were recorded. The quoted uncertainty in an individual TNR neural network electron density measurement is 2%–3%. Since there were generally at least 10 TNR measurements per FC spectrum, the uncertainty in the mean of the TNR measurements of  $n_e$ , or  $\sigma_e = \Delta n_e / \sqrt{N - 1}$ , is used for the uncertainty in  $n_e$ . Only FC spectra with  $N \geq 10$  were selected for this study.

The bottom panel in Figure 4-1 is a histogram of the distribution the uncertainties with which each component of (4.3) contributes to the overall uncertainty in  $F_m$ . In addition, the distribution of  $F_m$  itself is also plotted. It is clear that the uncertainty in  $n_\alpha$  does not strongly effect the calculation of  $F_m$ . The uncertainty in the proton number density is the next most significant factor, and the value for  $n_e$  measured by TNR has the largest average uncertainty. The average values of the uncertainties are  $\sigma_p = 1.0\%$ ,  $\sigma_\alpha = 0.004\%$ ,  $\sigma_e = 3.1\%$ , and  $\sigma_m = 3.5\%$ , which should be compared to the average value for  $F_m$  of  $\sim 6\%$ .

For values of  $F_m \leq 20$  the uncertainty in  $F_m$  is less than the average value of  $F_m$  itself, as is suggested by this figure and verified by plotting the ratio of  $\sigma_m/F_m$  for  $F_m \neq 0$ . It is telling that the portion of the histogram with values of  $F_m \geq 30\%$  overlaps exactly with the upper tail of the histogram of the total uncertainty in  $\sigma_m$  (and the distribution of  $\sigma_e$ , which dominates  $\sigma_m$  in this interval). The implication,

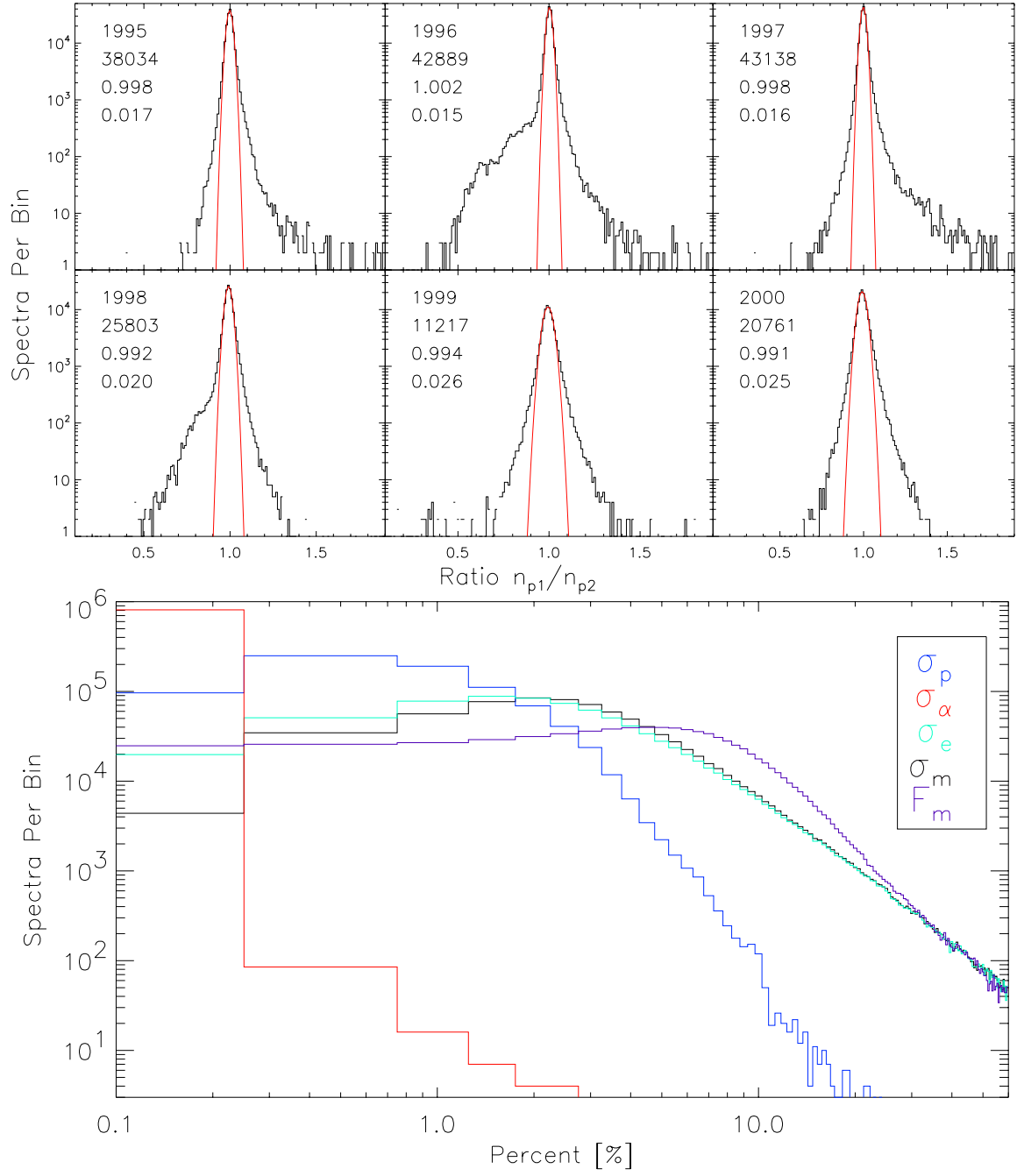


Figure 4-1: Predicted fraction  $F_m$  of the total electron number density due to minor ions as a function of proton bulk speed and year.

which was verified through a scatter plot to associate the points, is that the large departures of  $F_m$  from zero, which are rarely seen, are due to periods in the solar wind when the variation of the TNR electron number density was very large. The two in fact correspond exactly. The consequences of this are that very large values of  $F_m$  may be attributed to intervals with large fluctuations and a large resulting statistical uncertainty in  $F_m$ , and not due to periods when one instrument or the other is not functioning ideally. The other conclusion is that the variation of  $F_m$  is dominated by the fluctuation of the electron measurements from TNR, which are on the order of 3.1%. A spread in  $F_m$  on the order of 3.5% therefore would only reflect the variation of the electron number density measurements, and not any intrinsic error in the proton, alpha, or electron number densities.

We are not interested in comparing the instruments over the entire range of interplanetary conditions. Since the focus is on quiet periods where the values measured are more trustworthy the study is further restricted to spectra with  $\sigma_p \leq 5\%$ ,  $\sigma_\alpha \leq 1\%$ , and  $\sigma_e \leq 10\%$ . A total of 713,742 spectra, or 78% of the total dataset passed all of the cuts described in this section and were used for the study of  $F_m$ .

#### 4.4.2 Survey Over Mission

The median value of  $F_m$  over the entire selected dataset was 5.86%, with an average value of 6.36% and a standard deviation of 5.1%. The standard deviation is in agreement with the observations of [Maksimovic et al., 1998], although  $F_m$  is 4% larger than was reported in that same study. This can be attributed in part to the refined analysis of the TNR data since that study and to the fact that on average the proton number densities derived from the bi-Maxwellian analysis are about 1% smaller than the key-parameter number densities which were used in that study. We believe that the 1% shift in the FC number densities is due to the use of new effective area and response functions, as derived in Chapter 2.

The average value of  $F_m$  is slightly larger than the median value because there is an excess of observations on the  $F_m \geq 5\%$  side. In fact the distribution of the entire set of measurements does not appear to be exactly Maxwellian. We interpreted this as evidence that the overall histogram reflected the variation of  $F_m$  over a set of variables. Two factors which we believed could influence  $F_m$  are the bulk speed of the solar wind and the period in the solar cycle. Studies of minor ion charge states have demonstrated that statistically speaking the freeze-in temperature of the minor ions is cooler at higher solar wind speeds, and therefore less ionized. Additionally, the abundance of species other than protons reflects in part evolution of the corona material at the origin of the solar wind. Studies have shown that the helium abundance is an increasing function of speed. If the same process occurred with the other minor ions then it might be expected that the minor ion abundance at high speeds would be larger. The actual effect of these two competing processes on the  $F_m$  as a function of  $U_p$  is not clear, but we must take that possibility into account. Additionally the helium abundance has been demonstrated to vary over the course of the solar cycle. Therefore we decided to look at the distribution of  $F_m$  as a function of year from 1995-2000 and bulk proton speed.

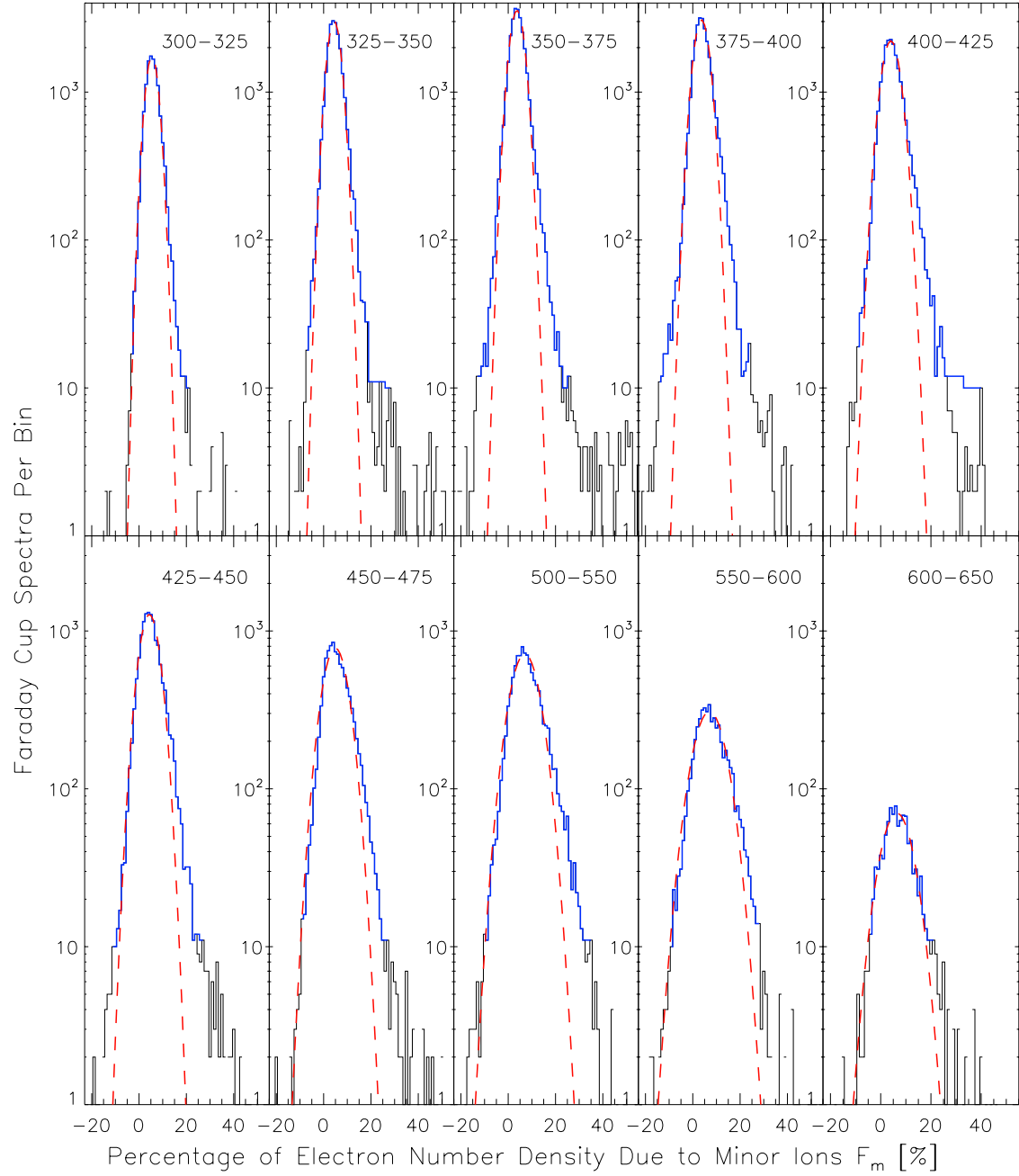


Figure 4-2: Histograms of  $F_m$  in six speed windows using selected data in 1995. Black histogram is the number of spectra observed per 0.5% bin in  $F_m$ , blue line is portion of the histogram selected for fit with Gaussian, and red is the best-fit Gaussian distribution. Note that the width increases with speed and that observations with  $F_m < 0$  are in agreement with tail of Gaussian.

For each year the selected observations were divided into ten intervals in speed ranging from 300 to 650 km/s. The first seven windows are 25 km/s wide. Since the number of measurements decreases with speed, the final three windows are 50 km/s wide to improve the statistics of the high speed intervals. The ten histograms of  $F_m$  as a function of speed window for 1995 are shown in Figure 4-3. In each histogram all intervals with more than 10 spectra were selected and fitted with a Gaussian probability distribution. The blue curves indicate the bins which were selected for fitting and the dashed red lines are the best-fit Gaussians.

Overall the Gaussians fit the observed distributions well. Several trends are worthy of comment. First note that in most cases the portion of each histogram with values of  $F_m < 0$ , an unphysical result, may be accounted for by the natural width  $\Delta F_m$  of the distributions. In other words if the  $\Delta F_m$  in part represent the overall uncertainty of  $F_m$  then it is natural for this amount of observations to have  $F_m < 0$ . Of course  $\Delta F_m$  is additionally due to the natural variation of the contribution to  $n_e$  from minor ions, and that variation can be estimated. Note as well that the  $\Delta F_m$  increase as a function of speed. Additionally, there appears to be a bias, or tail in many of the distributions at high values of  $F_m$ , suggesting that there are some intervals where  $F_m$  is enhanced beyond the simple Gaussian variation observed. Helium enhancements are often observed in the material associated with coronal mass ejections, for example, and the same rare effect may account for this tail, which is still small compared with the overall distribution.

The determination of the average value of  $F_m$  as a function of speed and year, and the estimate of the natural variation of the minor ion component, are detailed in Figure 4-3. In the upper panel colored solid lines indicate the width  $\Delta F_m$  of the best-fit Gaussian distributions to the observations as a function of speed for each year. The colored years printed at the top of the plot correspond to each of these curves. In general  $\Delta F_m$  increased linearly from about 1.5% to 3% as the speed ranged from 300-650 km/s. There is a suggestion of a time dependent increase in the width of the distributions in the speed range 375-475 km/s with solar cycle. The connected diamonds plotted in this panel are the average uncertainties of the proton, electron, and alpha particle contributions to  $n_e$  in each speed interval. It is clear that the total uncertainty  $\sigma_m$  in  $F_m$  derived from these individual uncertainties through (4.3) is dominated by the variation in the TNR electron measurements over each FC spectrum, and that  $\sigma_m$  is a decreasing function of  $U_p$ . According to the discussion in the previous section, we interpret  $(\Delta F_m^2 - \sigma_m^2)^{1/2}$  as the natural variation of  $F_m$  due to the variation of the abundance and charge state of the minor ions in the solar wind.

In the final panel of Figure 4-3 the center of the  $F_m$  distribution is plotted as a function of speed for each of the years from 1995-2000. Measurements in the same speed window have been offset by several km/s to avoid confusion. The horizontal error bars are the widths of the bins and the vertical error bars are the natural variations of  $F_m$  derived from the data in the upper panel. The two dashed lines indicate the two estimates of  $F_m$  in the introduction. There are variations in  $F_m$  with speed which should be compared with more detailed predictions. Additionally there appears to be a two-state distribution in the interval  $U_p \leq 425$  km/s, with

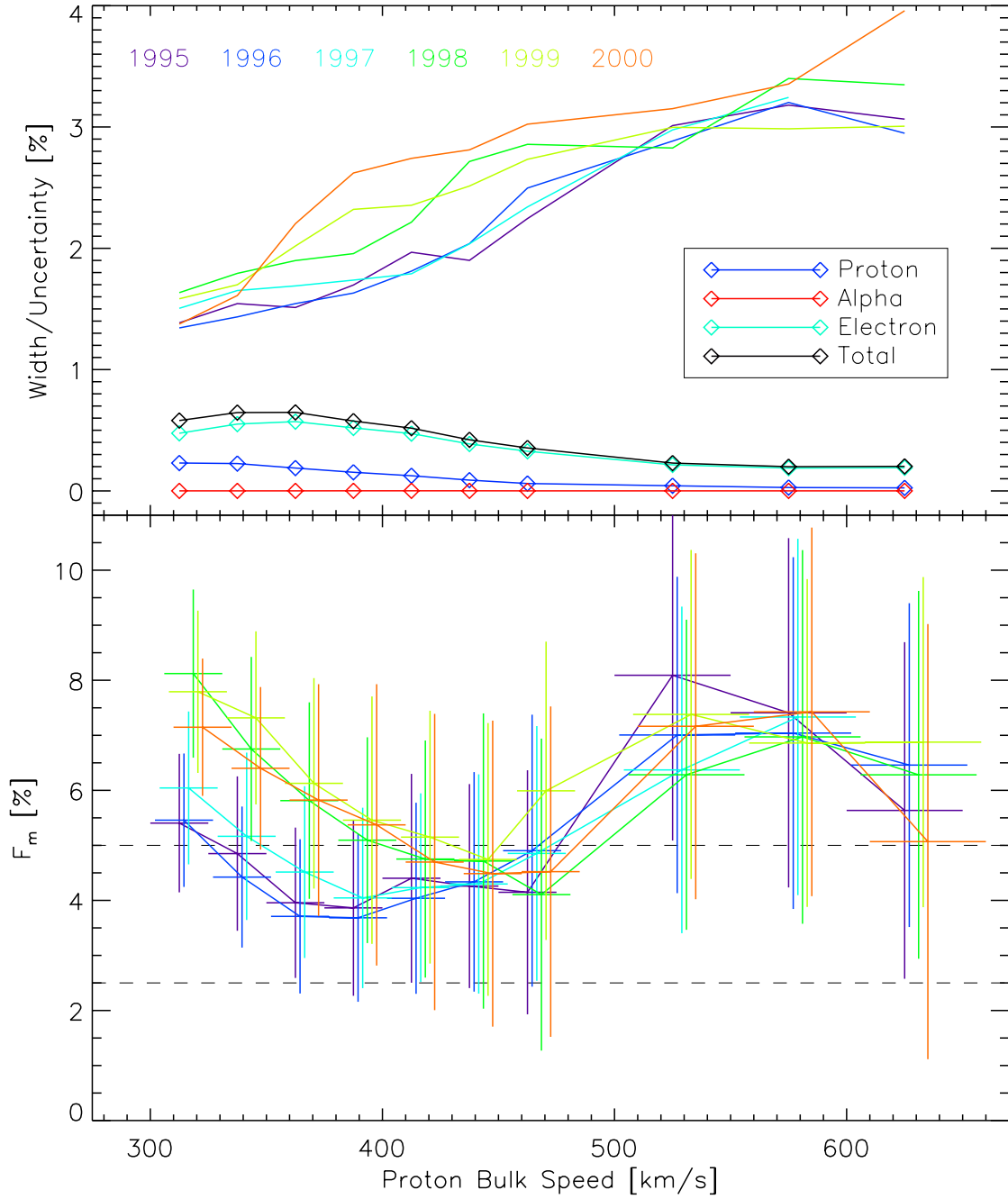


Figure 4-3: Predicted fraction  $F_m$  of the total electron number density due to minor ions as a function of proton bulk speed and year. *Upper panel:* Solid lines are the widths of the Gaussian fits to the distribution of  $F_m$  in each speed/year interval, connected diamonds are the corresponding average uncertainties in  $F_p$ ,  $F_\alpha$ , and  $F_e$ . *Lower panel:* Center of  $F_m$  distributions and natural widths as a function of speed and year. Dashed lines indicate estimates of the expected contribution of minor ions to the total electron number density.



all observations in 1995-1997 and in 1998-2000 falling into two distinct intervals. This could be a signature of the type of speed and solar cycle modulation which has been seen in the past with helium observations. For  $U_p \geq 500$  km/s  $F_m$  is consistently greater than the predicted values. This could be a reflection of the enhanced abundance of minor ions in high speed solar wind. But it might also reflect the fact that high speed solar wind often contains two proton distributions, and that this second proton distribution is not reflected in this analysis. A followup to this investigation should include the double streaming analysis currently being conducted by Dorian Clack.

In summary, the estimates of  $F_m$ , the TNR electron measurements, and the SWE/FC proton and alpha number densities agree to within a few percent. The widths of the  $F_m$  distributions are consistent with the derived uncertainties in the proton and alpha number densities being less than 1%. Furthermore the agreement between  $F_m$  and theory is consistent with the Wind Faraday Cups having correct and stable density calibrations within approximately 2% of the absolute values.

## 4.5 A Single Effective Ion Species

If a single fluid description of the solar wind is desired then it is necessary to merge the proton and alpha data to create an effective ion species. In Chapter 6 this single effective ion species will be used in the characterization of shocks through conservation of the MHD equations. The value of a single species for a treatment of kinetic processes is questionable, as this aspect is explored in Section 5.4. This section presents a derivation of the single fluid properties based on the method of reducing ion and electron data for the single fluid MHD problem outlined in Section 1.2.7. A valuable asset of the proton and alpha parameters derived from the Faraday Cup data are the one-sigma uncertainties which are produced during the non-linear fits. The goal of this section is therefore to derive the single ion parameters but in addition to propagate the uncertainties from the alpha and proton analysis.

The reduced ion species will have the same mass as the protons, so the number density  $n_i$  is just the total of the number of protons and neutrons,

$$n_i \equiv n_p + 4n_\alpha \quad (4.5)$$

with an accompanying uncertainty  $\sigma_{n_i}$  given by,

$$\sigma_{n_i}^2 = \sigma_{n_p}^2 + 16\sigma_{n_\alpha}^2. \quad (4.6)$$

For the bulk velocity use the velocity  $\vec{U}_i$  of the center of mass of the two ion species by weighting the individual proton  $\vec{U}_p$  and alpha  $\vec{U}_\alpha$  velocities by their mass densities,

$$\vec{U}_i \equiv \frac{n_p \vec{U}_p + 4n_\alpha \vec{U}_\alpha}{n_p + 4n_\alpha}. \quad (4.7)$$

The uncertainty in  $\vec{U}_i$  is a function of both species number densities and velocities. The uncertainty of the  $j^{\text{th}}$  component of the velocity,  $U_{i,j}$ , is given by,

$$\sigma_{U_{i,j}}^2 = \frac{1}{(n_p + 4n_\alpha)^4} (256n_\alpha^4\sigma_{U_{\alpha j}}^2 + 128n_\alpha^3n_p\sigma_{U_{\alpha j}}^2 + 8n_\alpha n_p^3\sigma_{U_{pj}}^2 + n_p^2(n_p^2\sigma_{U_{pj}}^2 + 16\sigma_{n_\alpha}^2(U_{\alpha j} - U_{pj})^2) + 16n_\alpha^2(n_p^2(\sigma_{U_{\alpha j}}^2 + \sigma_{U_{pj}}^2) + \sigma_{n_p}^2(U_{\alpha j} - U_{pj})^2)) \quad (4.8)$$

To determine the average thermal speed of the ions,  $w_i$ , I started with the individual pressures of the individual ion species,

$$P_p = n_p k_B T_p = \frac{1}{2} n_p m_p w_p^2, \quad P_\alpha = n_\alpha k_B T_\alpha = \frac{1}{2} n_\alpha m_\alpha w_\alpha^2, \quad (4.9)$$

combined them and then set them equal to the pressure which would be produced by the single ion,

$$\begin{aligned} P_i = P_{\text{tot}} = P_p + P_\alpha &= \frac{1}{2} m_p (n_p w_p^2 + n_\alpha m_\alpha w_\alpha^2) \\ &= \frac{1}{2} m_p (n_p w_p^2 + 4n_\alpha w_\alpha^2) \\ &= \frac{1}{2} m_i w_i^2 \end{aligned} \quad (4.10)$$

again using the fact that the ion has mass  $m_p$  we can solve for the thermal speed,

$$w_i^2 \equiv \frac{n_p w_p^2 + 4n_\alpha w_\alpha^2}{n_p + 4n_\alpha}, \quad (4.11)$$

and its associated uncertainty,

$$\begin{aligned} \sigma_{w_i}^2 &= \left( 16n_\alpha^2(4n_\alpha + n_p)^2\sigma_{w_\alpha}^2 w_\alpha^2 + 4(n_p^2\sigma_{n_\alpha}^2 + n_\alpha^2\sigma_{n_p}^2)w_\alpha^4 + (n_p^2(4n_\alpha + n_p)^2\sigma_{w_p}^2 \right. \\ &\quad \left. - 8(n_p^2\sigma_{n_\alpha}^2 + n_\alpha^2\sigma_{n_p}^2)w_\alpha^2)w_p^2 + 4(n_p^2\sigma_{n_\alpha}^2 \right. \\ &\quad \left. + n_\alpha^2\sigma_{n_p}^2)w_p^4 \right) \left[ (4n_\alpha + n_p)^3(4n_\alpha w_\alpha^2 + n_p w_p^2) \right]^{-1}. \end{aligned} \quad (4.12)$$

The dominant effect of the helium is to increase the particle mass density. The largest effects now neglected are the mass density of minor ions in the solar wind and the temperature of the electrons, which may contribute to the overall pressure. Since electrons have approximately the same temperatures as the ions in the solar wind, they generally have bulk velocities much less than their thermal widths and as a result do not contribute to the effective velocity, but can at times dominate the total pressure.

## 4.6 Summary

The analysis of the SWE/FC ion spectra has been extended to include the determination when possible of alpha parameters using the techniques developed by [Aellig et al., 2001b], but with a bi-Maxwellian distribution VDF for the alpha particles as well as the protons.

It has been shown that the the absolute precision of the FC number densities is off by less than a couple percent from the true values, and that the uncertainty in the densities is indeed on the order of a single percent.

In the following chapters the relative kinetic properties of protons and alphas in the solar wind are compared and their limits are explored. The usefulness of the single ion species derived in the previous section will be examined in terms of collisionless shocks and kinetic instabilities.

# Bibliography

- M. Abramowitz and I. A. Stegun. *Handbook of Mathematical Functions*. Dover Publications, New York, ninth edition, 1972.
- M. R. Aellig, A. J. Lazarus, J. C. Kasper, and K. W. Ogilvie. Rapid Measurements of Solar Wind Ions with the Triana PlasMag Faraday Cup. *apss*, 277:305–307, 2001a.
- M. R. Aellig, A. J. Lazarus, and J. T. Steinberg. The Solar Wind Helium Abundance: Variation with Wind Speed and the Solar Cycle. *Geophysical Research Letters*, 28: 2767, July 2001b.
- H. Alfvén. On the Existence of Electromagnetic-Hydrodynamic Waves. *Arkiv for Astronomi*, 29:1–7, 1943.
- B. J. Anderson, S. A. Fuselier, S. P. Gary, and R. E. Denton. Magnetic spectral signatures in the Earth’s magnetosheath and plasma depletion layer. *Journal of Geophysical Research*, 99:5877–5891, 1994.
- E. Antonucci, S. Giordano, and M. A. Doderio. Hydrogen and Oxygen Temperatures in Coronal Holes. *Advances in Space Research*, 25:1923–1926, 2000.
- J. A. Araneda, A. F. Vinas, and H. F. Astudillo. Proton core temperature effects on the relative drift and anisotropy evolution of the ion beam instability in the fast solar wind. *Journal of Geophysical Research, In Press*, page 1, 2002.
- W. I. Axford. The Interaction between the Solar Wind and the Earth’s Magnetosphere. *Journal of Geophysical Research*, 67:3791, September 1962.
- A. Barnes. Collisionless damping of hydromagnetic waves. *Phys. Fluids*, 9:1483, 1966.
- J. W. Belcher and R. Burchsted. Energy densities of Alfvén waves between 0.7 and 1.6 AU. *Journal of Geophysical Research*, 79:4765–4768, November 1974.
- D. B. Berdichevsky, R. P. Lepping, A. Szabo, and A. J. Lazarus. Estimation of interplanetary shock-normals using multispacecraft observations: Cases of shocks within minutes of magnetohydrodynamic discontinuities. In *American Geophysical Union, Spring Meeting 2001, abstract #SH42B-10*, page 42, May 2001.
- L. Biermann. Kometenschweife und solare Korpuskularstrahlung. *Zeitschrift Astrophysics*, 29:274, 1951.

- L. Biermann. Solar corpuscular radiation and the interplanetary gas. *The Observatory*, 77:109–110, June 1957.
- N. N. Bogoliubov. In J. de Boer and G. E. Uhlenbeck, editors, *Studies in Statistical Mechanics*, volume 1. North-Holland, Amsterdam, 1962.
- A. Bonanno, H. Schlattl, and L. Paternò. The age of the Sun and the relativistic corrections in the EOS. *Astronomy and Astrophysics*, 390:1115–1118, August 2002.
- J.-L. Bougeret, M. L. Kaiser, P. J. Kellogg, R. Manning, K. Goetz, S. J. Monson, N. Monge, L. Friel, C. A. Meetre, C. Perche, L. Sitruk, and S. Hoang. Waves: The Radio and Plasma Wave Investigation on the Wind Spacecraft. *Space Science Reviews*, 71:231–263, February 1995.
- H. S. Bridge. Solar cycle manifestations in the interplanetary medium. In *Proceedings of the International Symposium on Solar-Terrestrial Physics*, volume 1, pages 47–62, June 1976.
- H. S. Bridge, J. W. Belcher, R. J. Butler, A. J. Lazarus, A. M. Mavretic, J. D. Sullivan, G. L. Siscoe, and V. M. Vasyliunas. The plasma experiment on the 1977 Voyager mission. *Space Science Reviews*, 21:259–287, December 1977.
- M. Bzowski, H. J. Fahr, and D. Ruciński. Ionization-induced Heat Flow in Heliospheric Hydrogen: Virtues and Flaws of Hydrodynamic Treatments. *Astrophysical Journal*, 544:496–507, November 2000.
- I. H. Cairns, D. H. Fairfield, R. R. Anderson, K. I. Paularena, and A. J. Lazarus. Reply. *Journal of Geophysical Research*, 101:7679–7684, April 1996.
- S. Chandrasekhar. *Principles of Stellar Dynamics*. University of Chicago Press, Chicago, 1942.
- S. Chandrasekhar. Dynamical friction. i. general considerations: the coefficient of dynamical friction. *Astrophysical Journal*, pages 255–262, 1943.
- S. Chandrasekhar, A. N. Kaufman, and K. M. Watson. The stability of the pinch. *Proc. Roy. Cos. London., Ser. A*, 245:435, 1958.
- J. K. Chao, L. H. Lyu, B. H. Wu, A. J. Lazarus, T. S. Chang, and R. P. Lepping. Observations of an intermediate shock in interplanetary space. *Journal of Geophysical Research*, 98:17443–17450, October 1993.
- G. F. Chew, M. L. Goldberger, and F. E. Low. The boltzmann equation and the one-fluid hydromagnetic equations in the absence of particle collisions. pages 112–118, 1965.
- D. Clack, A. Lazarus, J. Kasper, and M. Kaiser. Wind SWE observations of proton double streaming and correlations with wave activity. In *American Geophysical Union, Fall Meeting 2001, abstract #SH21A-0734*, page A734, December 2001.

- D. Clack, A. J. Lazarus, and J. C. Kasper. A Statistical Study of Proton Double Streaming Observed by Wind/SWE. In *American Geophysical Union, Spring Meeting 2002, abstract #SH21C-07*, page C7, May 2002.
- S. R. Cranmer. New Insights into Solar Coronal Plasma Kinetics from UVCS/SOHO. *American Astronomical Society Meeting*, 31:871, May 1999.
- N. U. Crooker, T. E. Eastman, and G. S. Stiles. Observations of plasma depletion in the magnetosheath at the dayside magnetopause. *Journal of Geophysical Research*, 84:869–874, March 1979.
- P. B. Dusenbery and J. V. Hollweg. Ion-cyclotron heating and acceleration of solar wind minor ions. *Journal of Geophysical Research*, 86:153–164, January 1981.
- W. A. Dziembowski, G. Fiorentini, B. Ricci, and R. Sienkiewicz. Helioseismology and the solar age. *Astronomy and Astrophysics*, 343:990–996, March 1999.
- A. Eviatar and M. Schultz. Ion-temperature anisotropies and the structure of the solar wind. *Planet. Spa. Sci.*, 18:321, 1970.
- T. E. Faber. *Fluid Dynamics for Physicists*, pages 37–40. Cambridge University Press, Cambridge, 1995.
- R. P. Feynman. *Statistical Mechanics: A Set of Lectures*, pages 2–5. Addison Wesley, Reading, 1972.
- S. P. Gary. *Theory of Space Plasma Microinstabilities*. Cambridge University Press, Cambridge, 1993.
- S. P. Gary, B. E. Goldstein, and J. T. Steinberg. Helium ion acceleration and heating by Alfvén/cyclotron fluctuations in the solar wind. *Journal of Geophysical Research*, 106:24955–24964, November 2001.
- S. P. Gary, H. Li, S. O’Rourke, and D. Winske. Proton resonant firehose instability: Temperature anisotropy and fluctuating field constraints. *Journal of Geophysical Research*, 103:14567–14574, 1998.
- S. P. Gary, M. E. McKean, D. Winske, B. J. Anderson, R. E. Denton, and S. A. Fuselier. The proton cyclotron instability and the anisotropy/B inverse correlation. *Journal of Geophysical Research*, 99:5903–5914, 1994.
- S. P. Gary, J. Wang, D. Winske, and S. A. Fuselier. Proton temperature anisotropy upper bound. *Journal of Geophysical Research*, 102:27159–27170, 1997.
- P. R. Gazis, J. D. Mihalov, A. Barnes, A. J. Lazarus, and E. J. Smith. Pioneer and Voyager observations of the solar wind at large heliocentric distances and latitudes. *Geophysical Research Letters*, 16:223–226, March 1989.

- G. B. Gelfreikh, V. I. Makarov, A. G. Tlatov, A. Riehoakainen, and K. Shibasaki. A study of development of global solar activity in the 23rd solar cycle based on radio observations with the Nobeyama radio heliograph. II. Dynamics of the differential rotation of the Sun. *Astronomy and Astrophysics*, 389:624–628, July 2002.
- G. Gloeckler. Ion composition measurement techniques for space plasmas. *Review of Scientific Instruments*, 61:3613–3620, November 1990.
- H. Goldstein. *Classical Mechanics*. Addison-Wesley, Reading, second edition, 1980.
- R. J. Goldston and P. H. Rutherford. *Introduction to Plasma Physics*. Institute of Plasma Physics, Philadelphia, 1997.
- L. G. Golub and J. M. Pasachoff. *The Solar Corona*, pages 22–71. Cambridge University Press, Cambridge, 1997.
- K. I. Gringauz, V. V. Bezrukikh, V. D. Ozerov, and R. E. Rybchinskii. *Dokl. Akad. Nauk. SSSR*, 131:1301, 1960.
- C. J. Hanson and S. D Kawaler. *Stellar Interiors: physical principles, structure, and evolution*, pages 261–311. Springer-Verlag, New York, 1994.
- S. Hayakawa. *Cosmic Ray Physics: Nuclear and Astrophysical Aspects*, pages 688–704. John Wiley and Sons, 1969.
- C. Hoffmeister. Physikalische Untersuchungen an Kometen. II. Die Bewegungen der Schweifmaterie und die Repulsivkraft der Sonne beim Kometen 1942 g. *Zeitschrift Astrophysics*, 23:1–18, 1944.
- J. V. Hollweg. Heating and acceleration of the solar wind in coronal holes: cyclotron resonances. *Advances in Space Research*, 30:469–469, 2002.
- K. Huang. *Statistical Mechanics*, chapter 3-5. John Wiley and Sons, 1963.
- D. E. Huddleston, A. D. Johnstone, A. J. Coates, and F. M. Neubauer. Quasi-linear pitch angle and energy diffusion of pickup ions near Comet Halley. *Journal of Geophysical Research*, 96:21329, December 1991.
- P. A. Isenberg. Resonant acceleration and heating of solar wind ions Anisotropy and dispersion. *Journal of Geophysical Research*, 89:6613–6622, August 1984.
- P. A. Isenberg. Energy Diffusion of Pickup Ions Upstream of Comets (JGR 92 (A8) 1987). In *Comet Encounters*, page 32, 1998.
- J. D. Jackson. *Classical Electrodynamics*. John Wiley and Sons, third edition, 1999.
- S. Jurac, J. C. Kasper, J. D. Richardson, and A. J. Lazarus. On the Geoeffectiveness of Interplanetary Shocks. In *American Geophysical Union, Spring Meeting 2001, abstract #SH62A-10*, page 62, May 2001a.

- S. Jurac, J. C. Kasper, J. D. Richardson, and A. J. Lazarus. The geoeffective scale sizes of solar wind events. In *American Geophysical Union, Fall Meeting 2001*, abstract #SH31A-0705, page A705, December 2001b.
- S. Jurac and J. D. Richardson. The dependence of plasma and magnetic field correlations in the solar wind on geomagnetic activity. *Journal of Geophysical Research*, 106:29195–29206, December 2001.
- J. C. Kasper, D. Clack, A. J. Lazarus, and A. Szabo. High Time Resolution Plasma Measurements with WIND. In *American Geophysical Union, Spring Meeting 2001*, abstract #SH42B-08, page 42, May 2001a.
- J. C. Kasper, A. J. Lazarus, D. Clack, and S. Jurac. Wind/SWE Observations of the Role of Instabilities in CME Ejecta. In *American Geophysical Union, Spring Meeting 2002*, abstract #SH21A-08, page A8, May 2002a.
- J. C. Kasper, A. J. Lazarus, S. Gary, and A. Szabo. A Statistical Study of Proton Temperature Anisotropies Measured by Wind/SWE. In *American Geophysical Union, Fall Meeting 2001*, abstract #SH21A-0733, page A733, December 2001b.
- J. C. Kasper, A. J. Lazarus, and S. P. Gary. Wind/SWE observations of firehose constraint on solar wind proton temperature anisotropy. *Geophysical Research Letters*, in press, 2002b.
- J. C. Kasper, A. J. Lazarus, S. P. Gary, and A. Szabo. Solar Wind Temperature Anisotropies. In *Solar Wind 10 Conference*, July 2002c.
- J. C. Kasper, A. J. Lazarus, and P. Seelunagsawat. Wind/SWE Plasma Observations of Kinetic-Scale Magnetic Holes. In *American Geophysical Union, Spring Meeting 2002*, abstract #SH21C-06, page C6, May 2002d.
- P. J. Kellogg. Flow of Plasma around the Earth. *Journal of Geophysical Research*, 67:3805, September 1962.
- C. F. Kennel and H. E. Petscheck. Limit on stably trapped particle fluxes. *Journal of Geophysical Research*, 71:1–28, 1966.
- L. W. Klein, K. W. Ogilvie, and L. F. Burlaga. Coulomb collisions in the solar wind. *Journal of Geophysical Research*, 90:7389–7395, August 1985.
- L. D. Landau and E. M. Lifshitz. *Course of Theoretical Physics: Physical Kinetics*, volume 10. Pergamon Press, Elmsford, New York, second edition, 1981.
- G. Lapenta and J. U. Brackbill. Contact discontinuities in collisionless plasmas: A comparison of hybrid and kinetic simulations. *Geophysical Research Letters*, 23:1713, 1996.
- A. J. Lazarus, J. T. Steinberg, and R. L. McNutt. A low-mass faraday cup experiment for the solar wind. *Unknown*, 93:27078, 1993.



- R. P. Lepping, D. B. Berdichevsky, L. F. Burlaga, A. J. Lazarus, J. Kasper, M. D. Desch, C.-C. Wu, D. V. Reames, H. J. Singer, C. W. Smith, and K. L. Ackerson. The Bastille day Magnetic Clouds and Upstream Shocks: Near-Earth Interplanetary Observations. *Solar Physics*, 204:285–303, December 2001.
- R. P. Lepping, L. F. Burlaga, A. Szabo, K. W. Ogilvie, W. H. Mish, D. Vassiliadis, A. J. Lazarus, J. T. Steinberg, C. J. Farrugia, L. Janoo, and F. Mariani. The Wind magnetic cloud and events of October 18-20, 1995: Interplanetary properties and as triggers for geomagnetic activity. *Journal of Geophysical Research*, 102:14049–14064, July 1997.
- R. P. Lepping, A. Szabo, K. W. Ogilvie, R. J. Fitzenreiter, A. J. Lazarus, and J. T. Steinberg. Magnetic cloud-bow shock interaction: WIND and IMP 8 observations. *Geophysical Research Letters*, 23:1195, 1996.
- R.-F. Lottermoser, M. Scholer, and A. P. Matthews. Ion kinetic effects in magnetic reconnection: Hybrid simulations. *Journal of Geophysical Research*, 103:4547–4560, March 1998.
- M. Maksimovic, J.-L. Bougeret, C. Perche, J. T. Steinberg, A. J. Lazarus, A. F. Viñas, and R. J. Fitzenreiter. Solar wind density intercomparisons on the Wind spacecraft using WAVES and SWE experiments. *Geophysical Research Letters*, 25:1265, April 1998.
- E. Marsch, R. Schwenn, H. Rosenbauer, K.-H. Muehlhaeuser, W. Pilipp, and F. M. Neubauer. Solar wind protons - Three-dimensional velocity distributions and derived plasma parameters measured between 0.3 and 1 AU. *Journal of Geophysical Research*, 87:52–72, January 1982.
- D. C. Montgomery and D. A. Tidman. *Plasma Kinetic Theory*. Mc Graw - Hill, New York, 1964.
- J. T. Nolte, A. S. Krieger, A. F. Timothy, R. E. Gold, E. C. Roelof, G. Vaiana, A. J. Lazarus, J. D. Sullivan, and P. S. McIntosh. Coronal Holes as Sources of Solar Wind. *Solar Physics*, 46:303–322, 1976.
- Z. Němeček, J. Šafránková, O. Santolík, K. Kudela, and E. T. Sarris. Energetic particles in the vicinity of the dawn magnetopause. *Advances in Space Research*, 20:851–856, September 1997.
- K. W. Ogilvie, D. J. Chornay, R. J. Fitzenreiter, F. Hunsaker, J. Keller, J. Lobell, G. Miller, J. D. Scudder, E. C. Sittler, R. B. Torbert, D. Bodet, G. Needell, A. J. Lazarus, J. T. Steinberg, J. H. Tappan, A. Mavretic, and E. Gergin. SWE, A Comprehensive Plasma Instrument for the Wind Spacecraft. *Space Science Reviews*, 71:55–77, February 1995.
- K. W. Ogilvie, J. T. Steinberg, R. J. Fitzenreiter, C. J. Owen, A. J. Lazarus, W. J. Farrell, and R. B. Torbert. Observations of the lunar plasma wake from the WIND spacecraft on December 27, 1994. *Geophysical Research Letters*, 23:1255, 1996.

- E. Parker. Extension of the Solar Corona into Interplanetary Space. *Journal of Geophysical Research*, 64:1675, November 1959.
- E. N. Parker. Dynamical Instability in an Anisotropic Ionized Gas of Low Density. *Physical Review*, 109:1874–1876, March 1958a.
- E. N. Parker. Suprathermal Particle Generation in the Solar Corona. *Astrophysical Journal*, 128:677, November 1958b.
- E. N. Parker. The Hydrodynamic Theory of Solar Corpuscular Radiation and Stellar Winds. *Astrophysical Journal*, 132:821, November 1960a.
- E. N. Parker. The Hydrodynamic Treatment of the Expanding Solar Corona. *Astrophysical Journal*, 132:175, July 1960b.
- G. K. Parks. *Physics of Space Plasmas: An Introduction*. Addison-Wesley, 1991.
- G. Paschmann, A. N. Fazakerly, and S. J. Schwartz. Moments of plasma velocity functions. In G. Paschmann and P. W. Daley, editors, *Analysis Methods for Multi-Spacecraft Data*. ESA Publications Division, Noordwijk, 1998.
- R. K. Pathria. *Statistical Mechanics*, pages 43–55. Reed Elsevier, New Delhi, India, second edition, 1972.
- K. I. Paularena and A. J. Lazarus. Comment on 'Intercalibration of solar wind instruments during the International Magnetospheric Study' by S. M. Petrinec and C. T. Russell. *Journal of Geophysical Research*, 99:14777, August 1994.
- K. I. Paularena, G. N. Zastenker, A. J. Lazarus, and P. A. Dalin. Solar wind plasma correlations between IMP 8, INTERBALL-1, and WIND. *Journal of Geophysical Research*, 103:14601–14618, July 1998.
- R. P. Pfaff, J. E. Borovsky, and D. T. Young, editors. *Measurement Techniques in Space Plasmas: Fields*, volume 1 of *Geophysical Monograph 103*. American Geophysical Union, Washington, D. C., 1998a.
- R. P. Pfaff, J. E. Borovsky, and D. T. Young, editors. *Measurement Techniques in Space Plasmas: Particles*, volume 2 of *Geophysical Monograph 103*. American Geophysical Union, Washington, D. C., 1998b.
- T.-D. Phan, G. Paschmann, W. Baumjohann, N. Sckopke, and H. Luehr. The magnetosheath region adjacent to the dayside magnetopause: AMPTE/IRM observations. *Journal of Geophysical Research*, 99:121–141, 1994.
- W. H. Press, S. A. Teukolsky, W. T. Vetterling, and B. P. Flannery. *Numerical Recipes in C: The Art of Scientific Computing*. Cambridge University Press, Cambridge, second edition, 1999.
- A. Raichoudhuri. *The Physics of Fluids and Plasmas: An Introduction for Astrophysicists*. Cambridge University Press, Cambridge, first edition, 1998.

- F. Reif. *Fundamentals of Statistical and Thermal Physics*. McGraw Hill, 1965.
- I. G. Richardson and H. V. Cane. Signatures of shock drivers in the solar wind and their dependence on the solar source location. *Journal of Geophysical Research*, 98:15295, September 1993.
- J. D. Richardson. Thermal ions at Saturn - Plasma parameters and implications. *Journal of Geophysical Research*, 91:1381–1389, February 1986.
- J. D. Richardson, J. C. Kasper, A. J. Lazarus, K. I. Paularena, and A. Wallace. Solar Cycle Variation of Shocks in the Heliosphere. In *American Geophysical Union, Fall Meeting 2001, abstract #SH21B-01*, page B1, December 2001.
- P. Riley, Z. Mikic, J. A. Linker, R. Lionello, and A. J. Lazarus. The Large-Scale Variability of Solar Wind Streams. In *American Geophysical Union, Fall Meeting 2001, abstract #SH32A-0729*, page A729, December 2001.
- D. E. Robbins, A. J. Hundhausen, and S. J. Bame. Helium in the solar wind. *Journal of Geophysical Research*, 75:1178–1187, March 1970.
- B. Rossi and S. Olbert. *Introduction to the Physics of Space*. McGraw-Hill, New York, 1970.
- O. Santolík, J. Šafránková, Z. Němeček, J.-A. Sauvaud, A. Fedorov, and G. Zastenker. Two-point measurement of hot plasma structures in the magnetotail lobes. *Advances in Space Research*, 20:993–997, September 1997.
- M. Schwarzschild. *Structure and Evolution of the Stars*, pages 30–95. Dover Publications, New York, 1965.
- L. Spitzer. *Physics of Fully Ionized Gasses*. Interscience Publishers, New York, 1956.
- J. T. Steinberg, W. C. Feldman, R. M. Skoug, J. C. Kasper, A. J. Lazarus, and L. Alaoui. Characteristics of the Distant Magnetosheath: Wind Measurements at 45 to 80 Earth Radii. In *American Geophysical Union, Spring Meeting 2001, abstract #SM42D-12*, page 42, May 2001.
- J. T. Steinberg, A. J. Lazarus, J. T. Ogilvie, R. Lepping, J. Byrnes, D. Chornay, J. Keller, R. B. Torbert, D. Bodet, and G. J. Needell. WIND measurements of proton and alpha particle flow and number density. In *Solar Wind 8 Conference*, page 36, June 1995.
- J. T. Steinberg, A. J. Lazarus, K. W. Ogilvie, R. Lepping, and J. Byrnes. Differential flow between solar wind protons and alpha particles: First WIND observations. *Geophysical Research Letters*, 23:1183, 1996.
- T. H. Stix. *Waves in Plasmas*. Springer-Verlag, New York, 1992.
- A. Szabo. An improved solution to the 'Rankine-Hugoniot' problem. *Journal of Geophysical Research*, 99:14737, August 1994.

- M. Tátrallyay, M. I. Verigin, K. Szegő, T. I. Gombosi, K. C. Hansen, K. Schwingschuh, M. Delva, I. Apáthy, A. P. Remizov, and T. Szemerey. On the Distribution of Pickup Ions as Observed by the Vega Spacecraft at Comet Halley. *Advances in Space Research*, 26:1565–1568, 2000.
- J. T. Tanabe, J. C. Kasper, and A. J. Lazarus. Proton and Alpha Particle Temperature Anisotropies in the Solar Wind with the WIND/SWE Faraday Cup. In *American Geophysical Union, Spring Meeting 2001, abstract #SH31A-11*, page 31, May 2001.
- R. M. Thorne and B. T. Tsurutani. The generation mechanism for magnetosheath lion roars. *Nature*, 293:384–386, October 1981.
- B. T. Tsurutani, E. J. Smith, R. R. Anderson, K. W. Ogilvie, J. D. Scudder, D. N. Baker, and S. J. Bame. Lion roars and nonoscillatory drift mirror waves in the magnetosheath. *Journal of Geophysical Research*, 87:6060–6072, August 1982.
- T. W. J. Unti, M. Neugebauer, and B. E. Goldstein. Direct Measurements of Solar-Wind Fluctuations Between 0.0048 and 13.3 HZ. *Astrophysical Journal*, 180:591–598, March 1973.
- V. M. Vasyliunas. 12. Deep Space Plasma Measurements. In *Methods of Experimental Physics*, volume 98, pages 49–88, New York, 1971. Academic Press.
- A. F. Vinas and J. D. Scudder. Fast and optimal solution to the 'Rankine-Hugoniot problem'. *Journal of Geophysical Research*, 91:39–58, January 1986.
- D. R. Weimer, D. Ober, N. C. Maynard, W. J. Burke, M. R. Collier, D. J. McComas, and C. W. Smith. Variable time delays in the propagation of the interplanetary magnetic field. *Journal of Geophysical Research*, 107, 2002.
- D. Winske and N. Omid. *Computer Space Plasma Physics: Simulation Techniques and Software*, chapter Methods and applications, page 103. Terra Sci., Tokyo, 1997.
- P. H. Yoon. Electromagnetic fire-hose instability in a fully relativistic bi-Maxwellian plasma. *Physics of Fluids B*, 2:842–844, April 1990.